THERMOCHEMISTRY MEASUREMENTS IN NON-ISOBARIC FLOWS

A Dissertation

by

DEAN WILLIAM ELLIS

Submitted to the Office of Graduate and Professional Studies of
Texas A&M University
in partial fulfillment of the requirements for the degree of

DOCTOR OF PHILOSOPHY

Chair of Committee,	Adonios Karpetis
Committee Members,	Rodney Bowersox
	Eric Petersen
	Diego Donzis
Head of Department,	Rodney Bowersox

August 2017

Major Subject: Aerospace Engineering

ABSTRACT

The primary research objective of this study is to advance our understanding of flame suppression in supersonic flows by improving a technique capable of measuring the full thermochemistry in such non-isobaric reacting flows. This is achieved through two different channels: firstly, by further developing an incoherent Raman laser diagnostic technique capable of independently measuring temperature and density, and secondly, by analyzing and modifying an existing miniature supersonic burner (currently utilized as the test bed for the experiments). Vibrational Raman scattering is used to measure density and composition of major species (CO_2, O_2, CO, N_2, CH_4, and H_2O) while rotational Raman scattering is used to measure temperature. The independent measurements of density and temperature allow for the determination of pressure. This line imaging technique is applied to flows with very high strain rates and Reynolds numbers emanating from a miniaturized combustor. A matrix inversion method is incorporated into the laser technique to account for crosstalk in the vibrational spectra. Spectral sensitivity in the charged-coupled device (CCD) array is also introduced into the vibrational processing. Laser energy normalization and laser pulse synchronization are added to the experimental setup. Significant improvements in signal-to-noise ratio (SNR) are observed. A commercial computational fluid dynamics (CFD) code is utilized to model the flow inside the burner. Due to the burners complex geometry, a three dimensional computational domain is used at the expense of a detailed chemical approach. Burner configurations with short and long fuel injectors were studied. Results for the short injector show a flame attached at the tip of the injector while results for the long injector show no combustion taking place. Computational and experimental mole fraction distributions at the nozzle

exit are also compared. Results for both injector configurations demonstrate frozen flow in the external supersonic flow, suggesting configuration inside the burner needs to be modified for future use.

DEDICATION

To my family, for their never-ending support

ACKNOWLEDGMENTS

I would like to thank Alex Bayeh and Wenjiang Xu, two people that helped and taught me many things during my first few years in graduate school. Also I would like to thank all of my close friends and my family who have encouraged me throughout this journey.

CONTRIBUTORS AND FUNDING SOURCES

Contributors

This work was supported by a dissertation committee consisting of Professors Adonios Karpetis, Rodney Bowersox, and Diego Donzis of the Department of Aerospace Engineering and Professor Eric Petersen of the Department of Mechanical Engineering.

The information contained in the section denoted as previous work was research mostly done by Dr. Alexander Bayeh and presented in his dissertation.

All other work conducted for the dissertation was completed by the student independently.

Funding Sources

Graduate study was supported by a Graduate Assistant Research fellowship from Texas A&M University.

TABLE OF CONTENTS

Page

LIST OF FIGURES

FIGURE Page

LIST OF TABLES

TABLE Page

1. INTRODUCTION

1.1 Motivation

For more than 5 decades, NASA has funded hypersonic air breathing technology. As opposed to rocket propelled vehicles, air breathing hypersonic vehicles have the additional challenge of mixing fuel and oxidizer at supersonic velocities. For this reason, the majority of this research has been focused on propulsion and combustion efficiency. As shown on research done on the X-43 scramjet, the pressure inside the combustor exhibits the classical supersonic combustion mode: shock dominated combustion [1]. This extreme environment, characterized by large pressure and velocity gradients, displays flow time scales in the order of the chemical time scales. At these flow time scales, chemical reactions begin to be suppressed and can eventually result in flame extinction.

A non-intrusive technique capable of measuring the full thermochemistry in extreme environments, like the ones seen inside a scramjet combustor, is of great benefit to the scientific community. The proposed study will attack the problem of improving the accuracy of thermochemical measurements in non-isobaric flows through two different channels: firstly, by further developing an incoherent Raman laser diagnostic technique capable of independently measuring temperature and density, and secondly, by modifying an existing miniature supersonic burner (currently utilized as the test bed for the experiments).

Incoherent Raman spectroscopy has been used to measure flow properties for many years [2]. Nevertheless, its application to supersonic reacting flows has been limited. Experiments that utilize laser diagnostics to measure flow properties in supersonic reacting flows commonly make use of optical windows to access the test

section [3, 4, 5, 6], which hinder low signal techniques such as incoherent Raman.

Various methods for Raman processing are described in Raman literature. The Matrix Inversion method (MI) [7, 8, 9] consists of solving the matrix equation S=P(T)N, where S the signal vector, N is a vector of unknown species number densities, and P(T) is the temperature dependent matrix relating signal to species number density. The Spectral Fitting method (SF) [10] creates a spectral library of Raman transitions based on Placzek's theory of polarizability. A hybrid method [11] was proposed that combines the best aspects of these two methods and that also addresses the issues caused by the curvature of the spectral image. The hybrid method makes use of spectral libraries to determine the temperature dependency of the matrix in the MI method, thus reducing the number of necessary calibrations. In the present work we present a simplified version of the MI method.

Previous work in the current research group focused on developing a miniaturized supersonic burner which is optically accessible, allowing for the use of low level laser techniques, such as incoherent Raman scattering. Previous experiments done by [12] showed chemiluminescence to be prohibitive in terms of noise. To this end, the work presented here was done to improve the capability of measuring the full thermochemistry in supersonic non-isobaric reacting flows.

1.2 Objectives

1.2.1 Laser Diagnostics

The primary research objective of this study is to advance our understanding of flame suppression in supersonic flows by improving a technique capable of measuring the full thermochemistry in such non-isobaric reacting flows. Improvements were made to the Raman system originally setup by [12]. The system allows for independent measurements of density and temperature in flows were pressure is not known a

priori. Noise in flame environments rendered the technique unusable. Several steps were taken with the final goal of improving the SNR of the system.

- **Spectral crosstalk**: A matrix inversion method was developed to reduce noise resulting from crosstalk in the vibrational spectra. As the figure on page 20 will show, there are two sources of crosstalk between Raman Channels: crosstalk due to their spectral overlap, and crosstalk due to the curvature of the image. Both of these sources are taken into account through selection of proper calibration gases and solving the matrix equation developed here (equation 2.11).

- **Species sensitivity in array**: Previous measurements did not account for species sensitivity in the CCD array. It will be shown that spatial behavior (slit function) can vary up to 18% between species. New technique takes into account each species slit function.

- **System Timing**: The timing of the system was modified. Current setup is able to synchronize the exposure time of the CCD with the laser pulse. New setup decreases fluctuations of the laser position in the array. Triggering modifications as well as the addition of a pulse generator addressed this issue.

- **Energy Normalization**: Laser pulse energy normalization was introduced into the system, resulting in SNR improvements of up to 20%. New equipment added included a fast rise photodiode, a photodiode amplifier, and a boxcar averager.

- **Modification of density and temperature calculation**: Improvements to the processing of the vibrational and rotational spectra were made. These

include side normalization to known conditions as well as individual slit functions.

1.2.2 Miniature Supersonic Burner

A miniature supersonic burner [13] was studied and modified with the purpose of generating a flow that was more amenable to the laser diagnostic technique discussed in this dissertation.

- **Case study**: Performed CFD on the inside of miniaturized burner. Results showed a lack of proper mixing. More importantly, they provided a better understanding into the steps that need to be taken in order to transition the burner to the MILD regime.

1.3 Previous Work- Laser Diagnostics

The experimental setup can be seen in Figure 1.1 and a more detailed explanation can be found in [12]. The second harmonic of a Nd:YAG laser provided pulses of about 0.8 J at 10 Hz. The laser beam was first expanded to avoid any damage to the optics through the use of a telescope, comprised of a negative 300 mm plano-concave and a 500 mm plano-convex lens, from a diameter ($1/e^2$) of 9 mm to 15 mm. Laser-induced plasma sparks at the focused probe volume were avoided by using a single-leg pulse stretcher [14, 15, 16]. Sparks are detrimental to Raman cameras since they usually saturate the pixel well-depths. A solution to this problem is to extend the laser pulse in time, all while keeping the pulse energy constant. This was achieved by introducing a 50/50 beam splitter and a 16 ft optical delay line. The optical delay line widened the pulse duration in time from $\sim$ 9 ns to $\sim$ 16 ns (FWHM). The exact behavior of the laser pulses was not able to be captured due to the fast rise and long fall times of the photodiode used (4 ns and 140 ns, respectively) [12]. Nevertheless, the objective of the pulse stretcher of lowering the peak power is achieved.

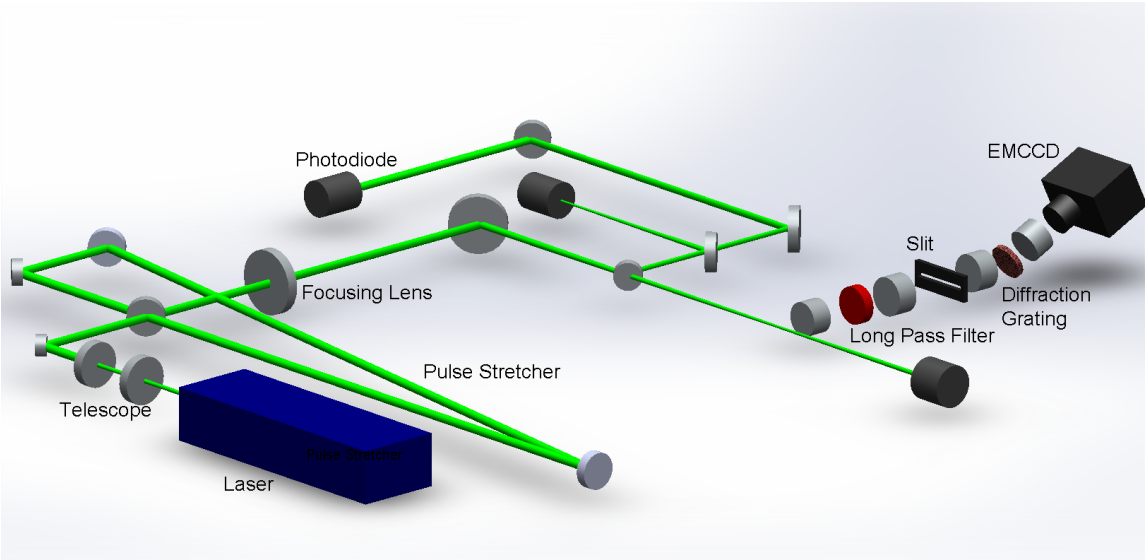

Figure 1.1: Illustration of the Raman imaging system. The laser pulses are first expanded in space by the use of a telescope. They are later expanded in time by the use of a pulse stretcher. The laser pulse focuses at the test section, where the signal is collected by a spectrometer composed of SLR lenses, a long pass filter, a slit, a transmissive diffraction grating and an EMCCD as the detector.

The laser beam was then focused using a 750 mm lens into a measuring volume with a diameter of approximately 0.195 mm ($1/e^2$). The light was collected by an axial transmissive Raman Spectrometer comprised of SLR lenses, a long pass filter, a 250 µm slit, and a transmissive diffraction grating.

An axial transmissive spectrometer was chosen over a Czerny-Turner configuration since it generates less aberrations and allows operation at very low f/numbers [17]. Similar transmissive configurations have been built in the past [11, 18, 19].The first optical relay of of the Raman spectrometer system is composed of a pair of 85-mm f/1.8 Nikkor lenses. The relative weakness of the Raman signal required the use of small f/numbers. A smaller f/number means a larger solid angle and therefore a greater amount of light collected. For instance, an f/1.8 collects about $(4/1.8)^2$ or 5 times more light than a f/4 lens [17]. A long pass filter was positioned in the

collimated region of the first optical relay. The filter is a Semrock razor-edge, with a nominal cutoff at 536 nm. The filter is necessary to block the rayleigh signal. A cutoff at 536 nm also filters a significant amount of rotational signal, so it was angle tuned to a wavelength closer to the laser's wavelength(532 nm) [20].

The slit was positioned between the first and the second optical relay and it determined the examined probe volume. The 250 µm thickness accommodated the waist of the laser (∼195 µm) and blocked excess background luminosity from reaching the detector. The light focused at the slit was then collected by the second optical relay, composed of a pair of 50-mm and 30-mm f/1.4 Sigma lenses. The different focal lengths chosen for the second optical relay result in a magnification factor on the images, as will be later explained. A smaller f/number was also chosen for the second optical relay to avoid any loss of signal. Dispersion of the collected signal was achieved by a holographic diffraction grating (Wasatch Photonics) positioned in the collimated region of the second optical relay. The incident and diffracted angles (ϕ_{inc} and ϕ_{diff}) of the grating can be calculated by well the known bragg equation [21]

$$m_B\lambda = \Lambda(sin\ \theta_{incident} + sin\ \theta_{diffracted}) \tag{1.1}$$

where m_B is the Bragg diffraction order, λ is the wavelength of the incident light, Λ is the spacing of the grating (inverse of dispersion). A dispersion of 1200 lpmm was chosen as a compromise between spectral range and crosstalk reduction. Examination of Equation 1.1 shows that the larger the dispersion, the larger the diffracted angle $\theta_{diffracted}$ and ergo, species are separated by a larger distance in the camera array. This dispersion is specially beneficial when examining molecules that are spectrally close to each other and suffer from spectral crosstalk such as N_2-CO and O_2-CO_2. However, the size of the camera array sets a boundary on how much

dispersion is possible before species begin to fall outside of the array. The grating has a central (blaze) wavelength of 600 nm and a dispersion of 1200 lpmm. The blaze wavelength was chosen to approximately match the center wavelength of the experiment's spectral range. This was done to assure the measured species were all close to the wavelength with the grating's peak diffraction efficiency, i.e. the blaze wavelength.

1.4 Previous Work- Miniature Supersonic Burner

The combustor used in the present study has been described in detail in [13] and only a brief description will be given here. A schematic of the present burner is shown in Figure 1.2. The burner consists of two stages: a vitiation stage and a second stage. The vitiation stage follows concepts found in early jet engine combustors [22, 23], in which air is divided into two streams before flame holding and ignition takes place. This configuration allows for operation of the vitiation stage at equivalence ratios below the flammability limits of the mixture, which increases the possible range of vitiation temperatures and species composition within the vitiation stage. For instance, a lean burning with an equivalence ratio of approximately 0.4, a value below the limit for methane-air flames, was utilized in the current experiments to ensure that excess air is present in the vitiated products and to avoid high temperatures that could potentially damage the device. The vitiated products and excess air coming out of the first stage then proceed to the second stage, where additional fuel ($Fuel_{ext}$) is added through an injector.

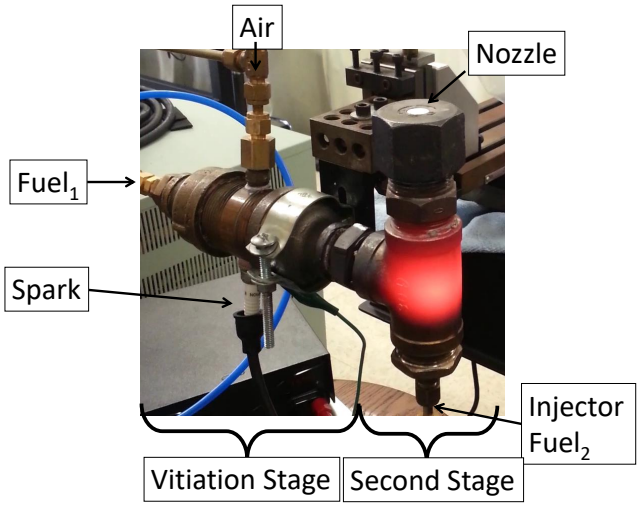

Figure 1.2: Schematic of the miniature supersonic burner. The burner has two stages: a vitiation stage and a stage where additional fuel is added. The air in the first stage is divided into two streams, allowing for burning to take place at values below the flammability limits of the mixture.

2. EXPERIMENTAL WORK

2.1 Laser Diagnostics

2.1.1 Signal-to-Noise Ratio in Measurements

The choice for the detector was a back illuminated, thermo-electrically cooled, with frame transfer capability EMCCD (Andor iXon). Electron multiplying CCDs offer significant improvement in Signal to Noise Ratios (SNR) under low light levels when compared to ICCD, EBCCD, or conventional CCD cameras [24]. The EMCCD used for the present study has multiple features that increase the SNR of measurements. The benefits can be clearly understood by analyzing the various sources of noise. The total noise (σ_t) present in a CCD camera is the result of shot noise (σ_s), dark current noise(σ_d), background noise(σ_b), and read noise(σ_r). The variance of the total noise (σ_t) is then given by

$$\sigma_t^2 = \sigma_s^2 + \sigma_b^2 + \sigma_d^2 + \sigma_r^2, \tag{2.1}$$

where it has been assumed that the sources of noise are independent from each other.

As a result of the statistical nature of photon detection, shot noise (σ_s) is described by Poisson statistics and thus equal to the square root of CCD signal ($\sqrt{S}$). The shot noise is an unavoidable source of noise and represents the theoretical noise limit of imaging devices. It is important to note that the signal (S) that gives rise to the shot noise (σ_s) refers to the number of photoelectrons generated from the Raman signal and not the Raman signal itself (S_R). To relate the Raman signal to Equation 2.1, the Quantum efficiency (Q) of the CCD needs to be considered. Quantum efficiency (Q)

represents the percentage of photons that are converted into photo-electrons. A back thinned, back illuminated sensor, like the e2v CCD97 utilized in this experiment, has close to 96% in Quantum efficiency. In contrast, a front illuminated sensor typically has values of 50% [25, 26][1]. The Raman signal (S_R) is then related to the CCD signal (S) by the Quantum efficiency (Q)

$$S = S_R Q \tag{2.2}$$

The Quantum efficiency affects the Background signal (B) in a similar manner. The background luminosity noise (σ_b), similarly to the shot noise, is also a Poisson process and equal to the square root of the Background Luminosity signal ($\sqrt{B}$). Background luminosity is caused by any type of incoming light that is not the Raman signal. Sources of light might include ambient light, laser-induced fluorescence, chemiluminescence, and radiation from soot and other particles. In flame environments, and specially in the spectral region of interest, the latter two sources of noise are the main contributors of background luminosity noise [2]. Since the background signal is integrated throughout the exposure time (τ), it is commonly expressed as a rate

$$B = \dot{B}\tau \tag{2.3}$$

Equation 2.3 shows that reducing the exposure time (τ) decreases this source of noise. The EMCCD chosen for this experiment is able to reduce the exposure time by having a frame transfer capability and fast vertical clocking. A simplified

[1]Etaloning is usually of concern when dealing with a back-thinned, back-illuminated CCD. Due to the small active layer thickness resulting from the thinning, constructive and destructive interference can occur whenever photons are reflected between the front and back faces of the active layer. However, etaloning appears in the NIR (> 700 nm), a spectral region that is beyond the wavelengths of the species measured in the current work, so it is not of concern [25, 27].

version of this architecture is shown in figure 2.1. A fast vertical clock allows the image to be transferred from the Image Area to the Storage Area in a short period of time, so that images can be read without accumulating any further background noise. The CCD array utilized in this experiment has an active area and storage area of 512x512 pixels each. A vertical speed of 0.5 µs and a 20 µs exposure were used, resulting in an effective exposure time (τ) of approximately 276 µs. Luminosity in flame environments is a major source of noise, which is why the exposure time is of such importance. Nevertheless, the fastest camera setting of 0.3 µs was not utilized because the Charge transfer efficiency would be significantly hindered. Charge transfer efficiency describes the amount of charge that is left behind when transferring charge between pixels, and it is decreased when a camera is clocked too fast. The 0.5 µs clocking speed was the fastest rate where no observed streaking was present. The effective exposure time of 276 µs is considerably longer than the experiments done by Sandia National Labs [28, 15] which utilize mechanical shutters. However, by not relying on the added infrastructure, the setup is substantially simplified.

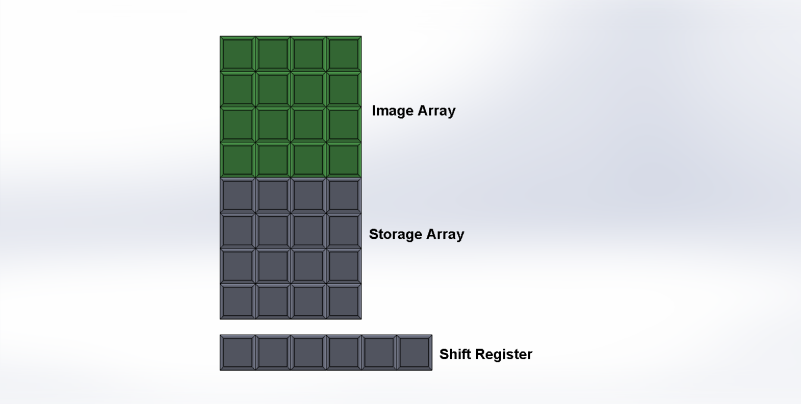

Figure 2.1: EMCCD architecture consists of an image array and a storage array. Exposed image can be vertically transferred to the storage array before readout commences. This architecture limits the exposure time and thus decreases background noise.

Dark current noise (σ_d) is a result of the dark current in the CCD. The stochastic nature of the dark current also makes it a Poisson process and therefore the dark current noise (σ_d) is equal to the square root of the dark current ($\sqrt{D}$). Dark current is produced by thermal excitation of electrons from the valence to the conduction band in the silicon substrate of the CCD, even in the absence of any signal [29, 24]. Therefore, it is strongly dependent on temperature. The thermo-electrically cooled EMCCD chosen for this experiment makes this source of noise negligible by cooling the camera down. Data was collected temperature of -100° C, a temperature low enough for dark current not to considerably contribute to the noise. In addition, dark current has an approximate linear dependence with the exposure time (τ) [29, 24]. The total dark current will be therefore given by the Dark current rate integrated over the exposure time

$$D = \dot{D}\tau \tag{2.4}$$

Taking into consideration the noise processes that are described by Poisson statistics, and additionally substituting in Equations 2.2- 2.4, Equation 2.1 can be rewritten as:

$$\sigma_t^2 = (QS_R + Q\dot{B}\tau + \dot{D}\tau) + \sigma_r^2, \tag{2.5}$$

where the Raman signal (S_R) was not given a rate dependence due to short life-time of Raman scattering ($\sim 10^{-11}$ [30]) relative to the exposure time of the image ($\sim$ 266 µs).

The read noise introduced by the amplifier is commonly the largest common source of noise for a conventional CCD [31].The read noise is strongly frame-rate dependent [32], therefore the slowest possible rate (1 MHz) was utilized to read out the images. The frame transfer capability allows the use of a slow reading rate

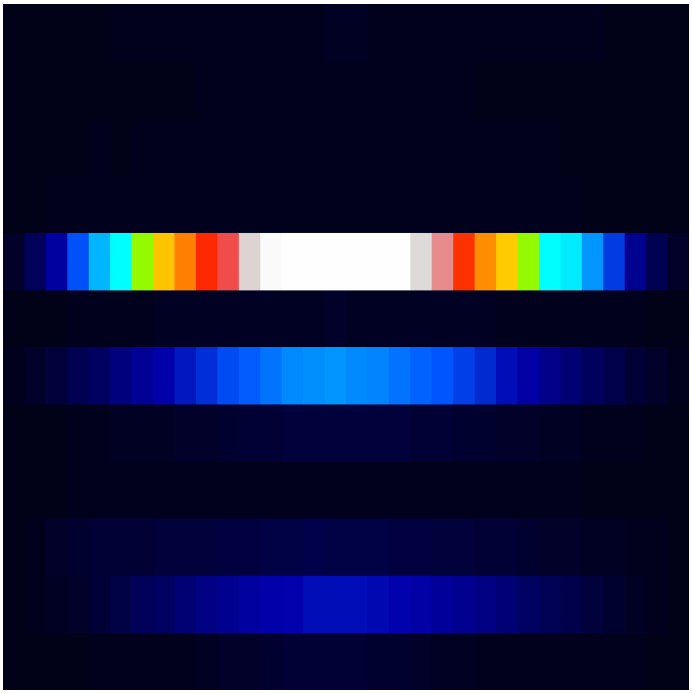

Figure 2.2: Sample measurement for spectra with hardware pixel binning. Only one vertical superpixel is used per species in order to reduce the read noise, while horizontal binning is kept at 16 to maintain spatial resolution.

without the compromise of added background luminosity. Additionally, EMCCD technology is able to reduce the read noise by introducing a gain register before the A/D converter. Since multiplication happens before the A/D conversion, signal is enhanced while keeping the read noise unchanged [33]. Consequently, the Signal To Noise Ratio (SNR) is considerably increased. The effect of the EM Gain (G) in Equation 2.5 can be seen through the use of the standard error propagation expression [34], which yields the following

$$\sigma_t^2 = \left(\frac{\partial^2 N_t}{\partial(QS_R)^2}\right)^2 \sigma_s^2 + \left(\frac{\partial^2 t}{\partial D^2}\right)^2 \sigma_d^2 + \left(\frac{\partial^2 t}{\partial(QB)^2}\right)^2 \sigma_z^2 \tag{2.6}$$

where the sources of noise are once again assumed to be independent. Applying Equation 2.6 to 2.5, one obtains

$$\sigma_t^2 = G^2QS_R + G^2QB + G^2D + \sigma_r^2 \tag{2.7}$$

where G is the Gain. Since the read noise is commonly the largest source of noise in a CCD, amplification of other noise sources at the expense of rendering the read noise is a beneficial trade-off for the SNR of the measurements. [2] On-chip hardware binning provides an additional measure to further increase the SNR of the system by suppressing the read noise. A sample measurement for spectra with hardware pixel binning can be seen in figure 2.2. Hardware binning adds charges of neighboring pixels before the A/D conversion. Similarly to the gain register, this means that read noise is injected only once per pixel grouping (superpixel). In low light imaging, like the present work, binning is a essential to obtain a good SNR. This, of course, comes at the expense of spatial resolution. To explicitly see the effect of hardware binning, Equation 2.7 can be rewritten, with the aid of the standard error propagation expression once more, as

$$\sigma_t^2 = M^2G^2QS_R + M^2G^2QB + M^2G^2D + \sigma_r^2 \tag{2.8}$$

where M is a multiplication factor resulting from binning M pixels together. The SNR equation can now be presented with the combined effects of hardware binning, EM Gain, and Quantum efficiency:

$$SNR = \frac{MGQS_R}{\sqrt{M^2G^2QS_R + M^2G^2QB + M^2G^2D + \sigma_r^2}} \tag{2.9}$$

To clearly see the effect of hardware binning (M) and EM Gain (G), Equation 2.9

[2] The stochastic nature of the process of Electron Multiplication also introduces an excess noise factor (F) that has been shown to approach $\sqrt{2}$ at high gains [24, 33].

can be simplified to

$$SNR = \frac{QS_R}{\sqrt{(QS_R + QB + D) + \left(\frac{\sigma_r}{MG}\right)^2}} \tag{2.10}$$

The final SNR equation explicitly demonstrates how when substantial Gain (G) is applied and sufficient pixels are binned together (M), the read noise (σ_r) becomes negligible. The frame transfer capability and the fast clocking reduce minimize the exposure time which reduces the background luminosity signal (B). The dark current is almost eliminated by thermo-electrically cooling the camera down to -100° C. Hardware binning, and EM Gain both are introduced with the sole purpose of rendering the read noise negligible. Consequently, noise in cold measurements is practically shot-noise limited while noise in flame environments is dominated by the background noise.

An Intensified CCD (ICCD) has the equivalent goal of suppressing the read noise by amplifying the signal. However, the manner in which this is achieved differs between them. An EMCCD relies on CCD architecture, performing electron multiplication while still retaining a high quantum efficiency and a relatively low excess noise factor. On the other hand, an ICCD relies on an external intensifier. External intensifiers are notorious for having high excess noise factors and low quantum efficiencies. Excess noise factors of 2-5 and quantum efficiencies of 45% are not uncommon in an ICCD[31]. However, their design allows for ultra fast acquisition rates. The good balance between SNR and speed made the EMCCD a better suited choice for this experiment.

2.1.2 Modifications to Spectrometer

As aforementioned, an axial configuration was chosen for the spectrometer, shown in figure 2.3. It is composed of two optical relays. Scattered light from the test section is first collected by an SLR lens with an 1.8 f-number (ratio of focal length to diameter of lens). The lower the f-number, the larger the solid angle and therefore the greater the amount of scattered light collected. The long pass filter is positioned in the collimated region of the first optical relay. Scattered light is then re-focused at the physical slit, which helps block excess background luminosity.

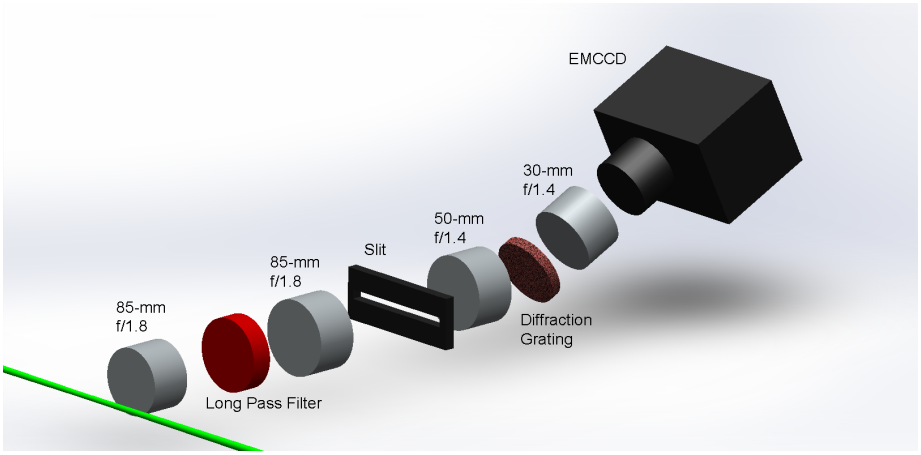

Figure 2.3: Axial spectrometer utilized in the present work. A long pass filter is positioned in the collimated region of the first optical relay while a diffraction grating is positioned in the collimated region of the second optical relay. An EMCCD was chosen as the detector.

Previous work had a pair of 30 mm, f/1.4 lenses as the second optical relay. For the current work, the first 30-mm lens was replaced with a 50 mm lens to increase the spatial range of the measurements. A 50-30 mm lens configuration magnifies the image by a factor of 5/3, resulting in a probe length of 13.65 mm as opposed to

the previous 8.192 mm. As will be described in the following sections, the current technique requires a known side condition in every shot for calibration purposes. This means that both the jet and ambient conditions have to be captured on the same shot. Even though the jet is only 3.5 mm in diameter, there is also an entrainment region that disturbs ambient conditions. Furthermore, the slit behavior of the image due to optical aberrations and laser de-focusing, as shown is figure 2.7, renders the pixels at the edge of the CCD array unusable.

Magnification of the system was evaluated against a target composed of five orifices with known distance between them. Table 2.1 compares the calibrated distance between the 5 orifices in the target to the distance as measured by the spectrometer. The magnification is shown to be within 6% of the theoretical value. It is important to note that this difference might be a result of a misalignment in any of the two optical relays, and thus careful alignment of the spectrometer should be done periodically.

Figure 2.4 shows a typical measurement done to check the accuracy of the calibrations. An N_2, O_2, CO_2 gas mixture with known composition flowing at subsonic speeds was measured. The addition of a 50-mm lens to the spectrometer, as well as the crosstalk calibrations, allow most of the array to produce usable data. Approximately 25 superpixels, or 400 pixels, along the laser axis display mole fractions with uncertainties of less than 10% of the known values. The effective length of the probe

Table 2.1: Spectrometer Alignment

	A	B	C	D
Actual distance	1562	1626	1550	1479
CCD measurement	928	976	880	848
Magnification	1.68	1.67	1.76	1.74

Units in micrometers

volume is therefore approximately 10.6 mm. This is in contrast with previous work, which had an effective probe length of about 4 mm. The sufficiently long enough length probe volume is necessary to perform side ambient normalization on a shot to shot basis, as explained in the following section.

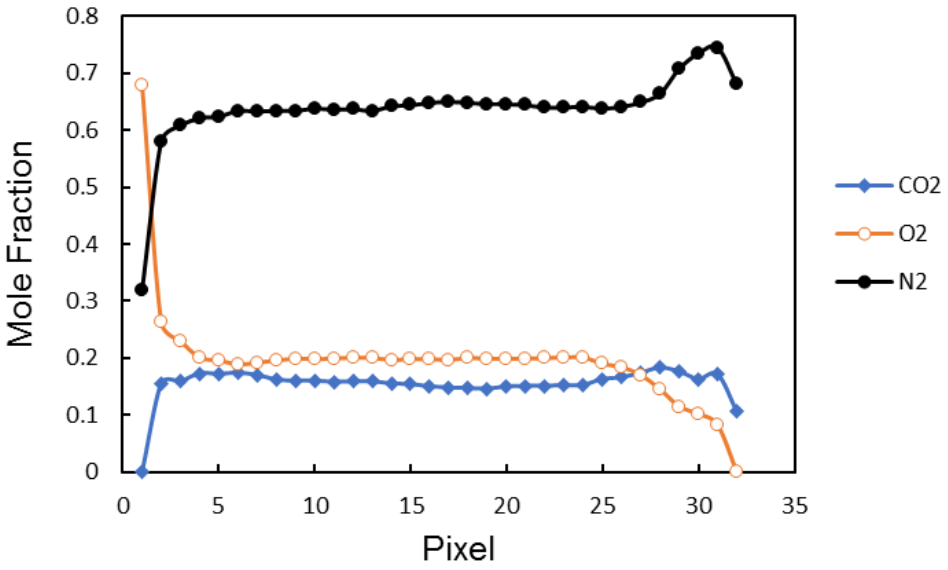

Figure 2.4: Measured average mole fractions for a N_2, O_2, CO_2 gas mixture at subsonic speeds. The addition of a 50-mm lens, as well as crosstalk calibrations, increase the effective length of the probe volume to about 25 superpixels, or 10.6 mm.

2.1.3 Spectral Crosstalk

Various methods for Raman processing are described in Raman literature. The Matrix Inversion method (MI) [7, 8, 9] consists of solving the matrix equation S=P(T)N, where S the signal vector, N is a vector of unknown species number densities, and P(T) is the temperature dependent matrix relating signal to species number density. In the matrix P(T), the diagonal terms represent the Raman re-

sponses of the various species, while the non-diagonal terms represent the crosstalk terms. The Spectral Fitting method (SF) [10] creates a spectral library of Raman transitions based on Placzek's theory of polarizability. The spectral library is then calibrated against gases of known composition and temperature. Composition can then be calculated by fitting the spectral signals to the spectral library. This method reduces the amount of calibrations to only one per species and automatically takes into account spectral crosstalk. However, spectral resolution hinders read noise suppression, and additionally significant effort is required to fit the Raman spectra to the single-shot measurements. A hybrid method [11] was proposed to combine the best aspects of these two methods and also to deal with the image curvature. The hybrid method makes use of spectral libraries to determine the temperature dependency of the matrix in the MI method, thus reducing the number of calibrations. To account for the image curvature, the signal is integrated several times while moving the pixel boundaries. A drawback of this hybrid approach is that it still relies on spectral fitting. This paper presents a variation of the hybrid method in which a matrix inversion is utilized to account for crosstalk and image curvature on the vibrational signal, while spectral fitting is used only on the rotational signal.

A close examination of Figure 2.5 shows two sources of crosstalk between Raman channels: crosstalk due to their spectral overlap, and crosstalk due to the curvature of the image. The two sources of crosstalk were handled by running calibrations and solving the following equation

Figure 2.5: Average sample measurement for high resolution spectra. Shown in the figure, from the top to bottom, are the vibrational Raman signals for CH_4, N_2, CO_2, and the rotational Raman spectra of the mixture. The curvature of the signal is evident and a major source of noise in the measurements.

$$\begin{bmatrix} E_{B3} \\ E_{N_2} \\ E_{CO_2} \\ E_{B4} \\ E_{O_2} \\ E_{CO_2} \\ E_{B5} \end{bmatrix} = \begin{bmatrix} 1 & 0 & 0 & 0 & 0 & 0 & 0 \\ 1 & 1-\gamma & \delta & 0 & 0 & 0 & 0 \\ 0 & \gamma & 1-\delta & 1 & 0 & 0 & 0 \\ 0 & 0 & 0 & 1 & 0 & 0 & 0 \\ 0 & 0 & 0 & 1 & 1-\beta & \alpha & 0 \\ 0 & 0 & 0 & 0 & \beta & 1-\alpha & 1 \\ 0 & 0 & 0 & 0 & 0 & 0 & 1 \end{bmatrix} \begin{bmatrix} E'_{B3} \\ E'_{N_2} \\ E'_{CO_2} \\ E^*_{B4} \\ E'_{O_2} \\ E'_{CO_2} \\ E'_{B5} \end{bmatrix} \tag{2.11}$$

Where E_i is the energy of the superpixel of species i, E'_i is the energy of species i if no crosstalk were present, B_i denotes the various background channels, and α, β, γ, δ are the crosstalk coefficients. It was assumed that signal overlap is only present between N_2-CO and O_2-CO_2. Furthermore, it was assumed that all of the Raman signal was captured by their corresponding species superpixel and none of it spilled

over to the background channels. Background luminosity was taken into account by subtracting each Raman channel with its nearest spectral background. A lack of a mechanical shutter greatly enhances the amount of background signal our system captures [28, 15], thus this subtraction is necessary. The calculation of the crosstalk coefficients is done through calibration. For instance, the α coefficient, shown in Figure 2.6, was calculated by running a mix of N_2 and CO_2 of known composition. Solving the matrix equation for this specific mix yields

$$\alpha = \frac{E_{O_2} - E_{B4}}{E'_{CO_2}} \tag{2.12}$$

where

$$E'_{CO_2} = (E_{O_2} - E_{B4}) + (E_{CO_2} - E_{B5}) \tag{2.13}$$

Given that this specific gas calibration did not have any O_2, the total CO_2 energy (E'_{CO_2}) is obtained by adding the energy of the CO_2 track and whatever energy spilled into the O_2 track. This addition has to be done since the superpixels are hardware binned and set at the beginning of each experiment. A similar procedure is followed to calculate the additional three crosstalk coefficients. The β coefficient is calculated by running a gas mixture that contains O_2 but no CO_2. This could be achieved even by ambient shots. Solving the matrix equation for this coefficient yields

$$\beta = \frac{E_{CO_2} - E_{B5}}{E'_{O_2}} \tag{2.14}$$

where

$$E'_{O_2} = (E_{O_2} - E_{B4}) + (E_{CO_2} - E_{B5}) \tag{2.15}$$

Figure 2.6 shows one crosstalk coefficient for a typical set of calibration gases. The α coefficient represents the amount of CO_2 spilled over to the O_2 track. The

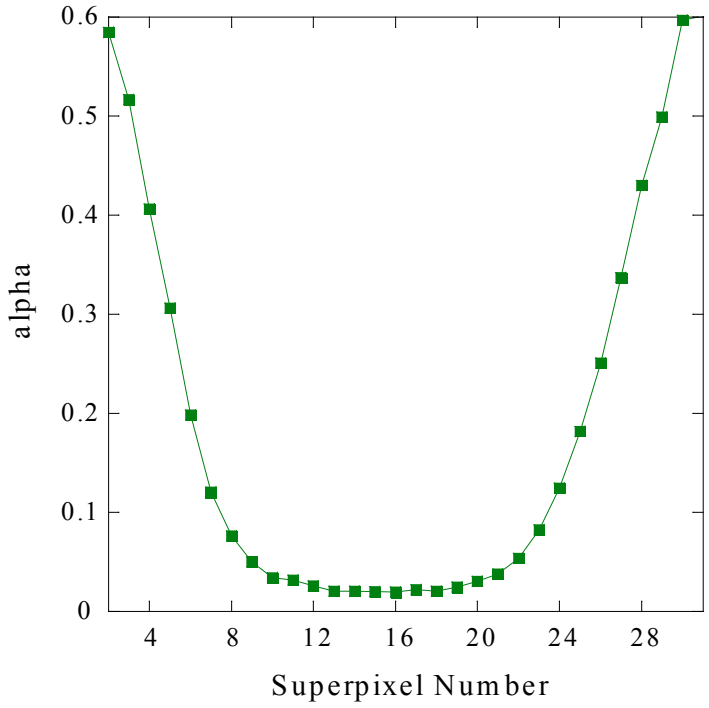

Figure 2.6: Crosstalk coefficient for the CO_2-O_2 crosstalk. Hardware binning and image curvature result in crosstalk being the largest at the sides of the array.

large α values on the sides of the array imply that a large portion of the CO_2 signal was spilled into the O_2 track. Conversely, a small α value means that little CO_2 was spilled over into the O_2 track. The shape of the graph is a result of the curvature of the image. Conversely, the β coefficient represents the amount of $O2$ signal that was spilled over to the CO_2 track. These coefficients inherently contain the crosstalk due to spectral location and due to the curvature of the image, which eliminates the need for spectral fitting to account for signal curvature on the CCD array. Temperature dependence is not taken into account in these calibrations.

2.1.4 Species Sensitivity in EMCCD Detector

The vibrational/rotational Raman technique relies on the measurement of signal from the Q-branch/S-branch Stokes lines of all major species (CO_2, O_2, CO, N_2, CH_4, H_2O) within every superpixel of the probe volume. Raman scattering is proportional to species concentration and may be described through the following phenomenological formula, applicable to both vibrational and rotational signals [2]

$$E_i^{'} = \epsilon \frac{n}{V} X_i l \omega \left[\frac{\partial \sigma}{\partial \omega}\right]_i E_l \tag{2.16}$$

where n is the total number of moles, V is volume (hence $C = n/V$ is the total molar density), X_i is the major species molar fractions, l the superpixel measurement length along the laser axis, ω the solid angle of light collection, $(\partial\sigma/\partial\omega)_i$ the differential scattering cross sections, E_l the laser pulse energy, and ϵ an overall optical system efficiency. The introduction of a physical slit as well as optical aberrations resulting from the off-axis configuration of the spectrometer introduce a spatial dependence on the Raman signal according to

$$E_i^{'}(\lambda, x) \; = \; S_i(x) \epsilon \frac{n}{V} X_i l \omega \left[\frac{\partial \sigma}{\partial \omega}\right]_i E_l \tag{2.17}$$

where $S_i(x)$ is defined as the slit function and describes the behavior of the Raman signal across the CCD array. Calculation of species specific slit functions through calibration allows us to normalize data measurements in order to minimize the spatial dependence of the spectral signal. Previous work [12] assumed that $S(x)$ varied only along the laser axis. It has been determined that this assumption introduces substantial error on the edges, thus the slit function is allowed to be a function of space and wavelength (species).

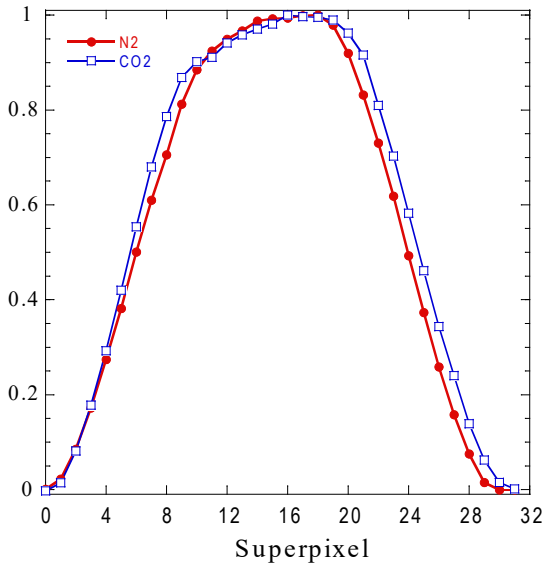

Figure 2.7: Slit functions for N_2 and CO_2 normalized by their respective maximum. The introduction of a physical slit alters the response of the system by blocking light in the regions where the laser focuses and de-focuses as shown.

Figure 2.7 shows $S_{N2}(x)$ and $S_{CO_2}(x)$ normalized by their respective maximum. Between superpixels 7-11 and 20-28, the the slit difference between these two molecules is as high as 18%. To avoid this source of error, species dependent slit functions were calculated by calibration of quiescent flow mixtures at known compositions. The difference in slit functions between species can be attributed to the vignetting of the optical system, as well as wavelength dependence of the transmissive grating and the CCD array.

Species molar fractions (X_i) are readily obtained by making use of equation 2.17. The calculation of molar or mass density (C or ρ), however, relies on absolute referencing to a known condition in a shot to shot basis. This is achieved by assuring the laser probe volume captures a known condition at every shot, such as ambient air at standard temperature and pressure conditions (STP). To this end, the jet is

positioned at an off center location at either side of the probe volume so that the CCD array is able to capture both the jet and the ambient air condition on the same shot. Even though this requirement places a big restriction on the diameter of the flow to be examined, the technique allows for absolute density measurements in non-isobaric flows where pressure is not known a priori.

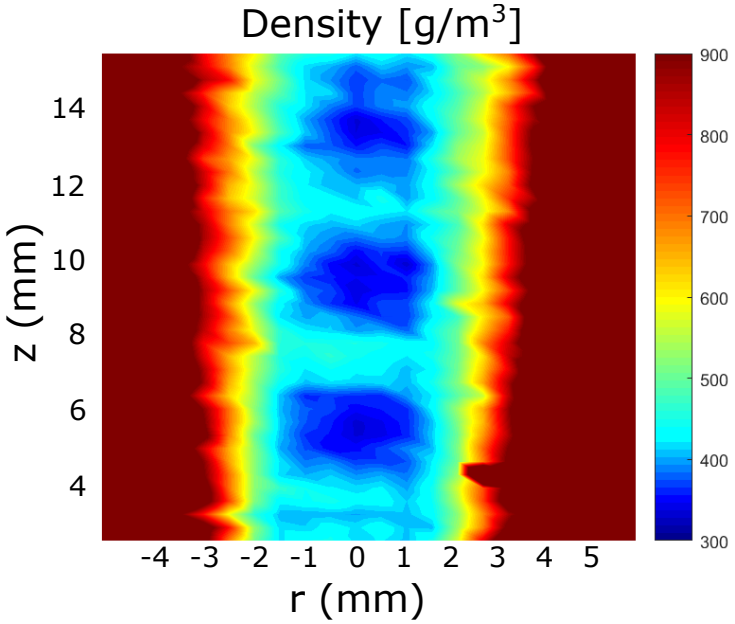

Figure 2.8: Averaged density values of an underexpanded vitiated jet. The increase in effective length of the probe volume allows for side normalization on a shot to shot basis.

Figure 2.8 displays how modifications done to the spectrometer as well as the introduction of a spectral crosstalk procedure improve measurements. The addition of a 50-mm lens in the second optical relay of the spectrometer allows each pixel to capture a length of 26 µm, compared to the 16 µm if a 1 to 1 imaging ratio had been preserved. Furthermore, the calibration procedure for spectral crosstalk and species array sensitivity attenuate the effect of curvature and decreased laser energy

at the periphery of the CCD array. The effective probe length volume is therefore increased from about 4 mm to approximately 10.4 mm. Previous measurements were limited to data obtained only at the center of the array, where the slit function was approximately constant in value.

2.1.5 System Timing

The settings of the EMCCD were set to a vertical clock speed of 0.5 µs and a horizontal readout rate of 1 MHz. The image size was 512 by 512 pixels, with a calibrated spectral resolution of 0.4016 nm per pixel. All images were dark noise subtracted, where the dark noise was an average of 50 images taken at the same EM setting and the same binning as the data. Images were also normalized by the local laser intensity, measured by the photodiode, to account for any laser energy fluctuations.

A Nd:YAG laser is used in conjunction with a pulse/delay generator, a boxcar averager, a photodiode, a photodiode amplifier, a data acquisition board, and an EMCCD camera to sync each laser pulse photodiode energy measurement with its corresponding camera image. The timing of the experimental setup is governed by the laser. As shown in figure 2.9, the pulse generator is triggered by the negative edge of the flash lamp discharge signal. The output of the pulse generator is then used to trigger the EMCCD. The output of the pulse generator does not necessarily agree in time with the Q-switch signal (laser pulse). In this particular system, the pulse from the pulse generator is delivered approximately 30 µs before the Q-switch signal. The 30 µs is enough time for the EMCCD clean cycle to be completed and for camera to get ready for exposure. Minimum exposure time of the specific EMCCD used in the present experiments corresponds to 10 µs. However, a 20 µs exposure is used to accommodate any variations in time from the EMCCDs fire signal. During

exposure time, vertical clocking of the CCD stops and the image builds up in the image array. Syncing the laser pulse with the CCD exposure time allows the laser signal to consistently land at the same row of pixels every shot, improving the overall SNR of the measurements. The end of the exposure time of the camera (fire signal) is then used to trigger the DAQ, which then reads the image from the camera.

The energy from each laser pulse is captured by a photodiode. A photodiode amplifier amplifies the analog signal and is recorded by a boxcar averager, which is triggered by the laser variable Q-switch. [3] The Last Sample Out (LSO) from the boxcar, or equivalently the average of a single image, is transmitted to one of the channels of the DAQ board. This configuration allows for the photodiode laser energy to match the corresponding camera image.

[3]Q-switch variable corresponds to a signal that can be adjusted to occur up to 175 ns before the Q-switch signal

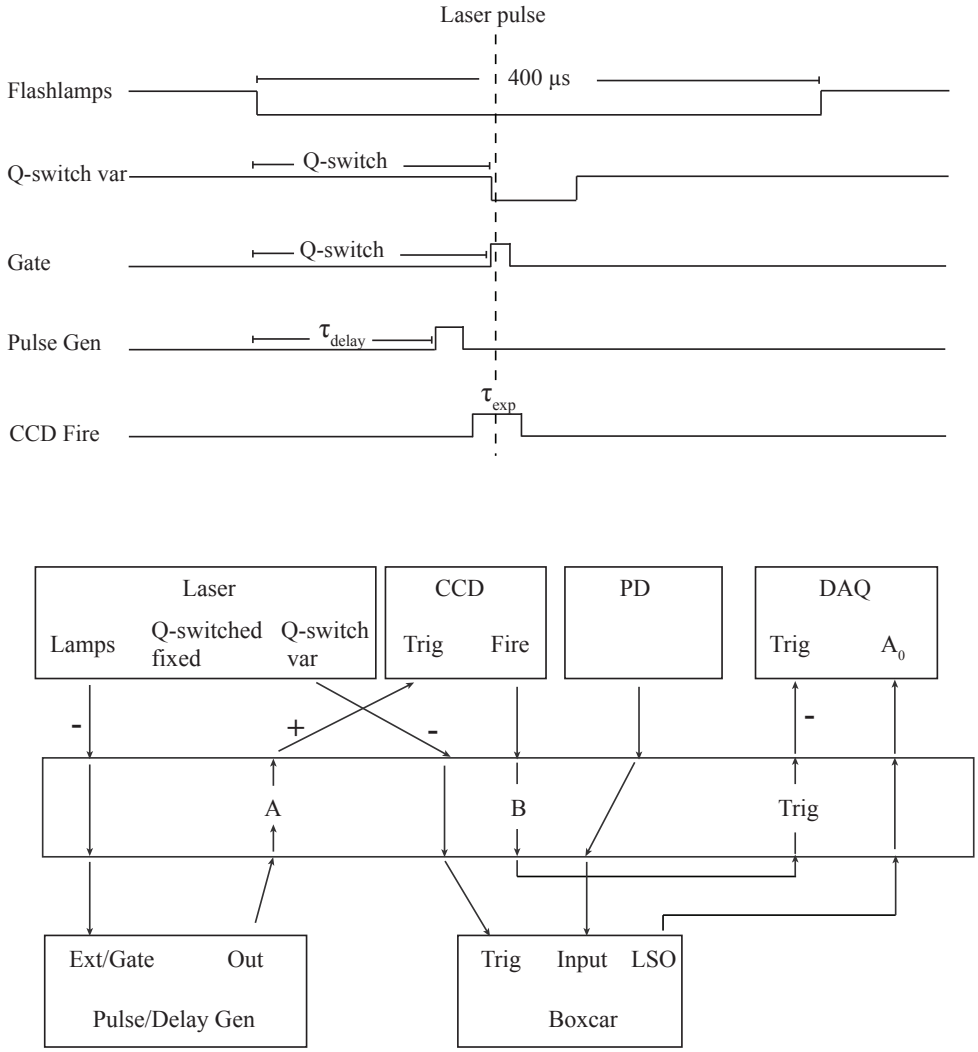

Figure 2.9: Timing diagram and schematic for the laser system. The laser lamps discharge signal and the Q-switch are utilized to eventually trigger the CCD and the Boxcar Averager.

2.1.6 Energy Normalization

Signal-to-noise ratios (SNR) of measurements done during previous work for air jets displayed values as low as 8.6 for nitrogen species mole fraction [12]. The SNR for a weaker signal, such as water, displayed values as low as 1.3. These values are

even lower when measuring a vitiated flow. One of the improvements done to the Raman system previously developed was the addition of an energy normalization system. Even though previous work assumes laser energy normalization in the data, functioning of the previous normalization system was intermittent at best.

Laser energy (E_o) is measured through the use of a photodiode, photodiode amplifier, and a boxcar averager. A fast rise (65 ns) photodiode with a large active area measures the energy of each laser pulse. This is done by capturing the reflection of the laser from one of the optics. The use of neutral density filters assures that the photodiode is not saturated. Analog signal from the photodiode is amplified with the use of a bench top amplifier. The amplifier used in the present setup is ideally suited for amplification of very small photodiode currents with little noise addition.

The fast analog signal generated by the photodiode amplifier is then read by the boxcar averager. The boxcar integrates the input signal over the duration of the sampling gate, which is manually set to capture the rise and fall of the photodiode. The boxcar then normalizes the integrated signal by the size of the gate to produce a voltage that is proportional to the average input signal. As stated in the previous section, the boxcar averager is externally triggered by the laser variable Q-switch signal. This energy normalization setup allowed the SNR of species mass fractions to be increased by up to 20%.

2.1.7 Density and Concentration Calculation

The calculation of density through the use of stokes vibrational spectra is outlined in figure 2.10 and described in what follows. Measurements from calibration gases are utilized to populate matrix M in equation 2.11 by solving for the crosstalk coefficients: α, β, γ, and δ. Calibration measurements also provide the slit functions of each species. As previously shown, slit functions can have variations of up to 18% between

species; previous work assumed only one slit function, given by the nitrogen signal. Careful selection of calibration gas mixtures allows for isolation of spectra to avoid crosstalk noise. For instance, a gas mixture of $CO2-CO$ allows for the calculation of each of these species slit function without concern about crosstalk noise given their large spectral separation. Furthermore, this calibration will inherently account for the curvature of the spectral image as well as the spectral sensitivity of the array.

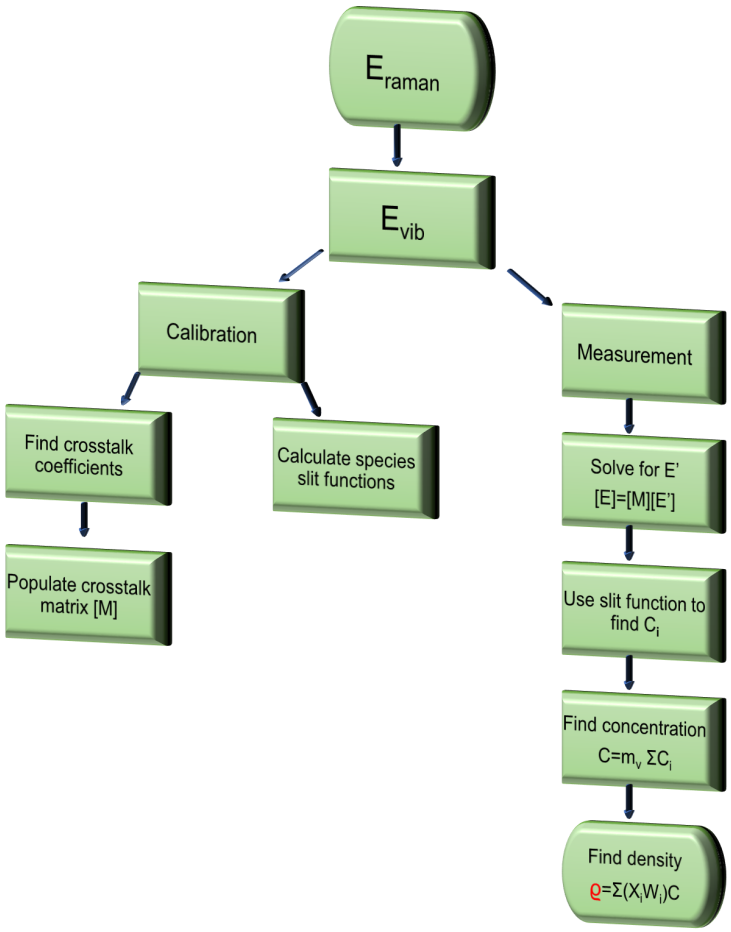

Figure 2.10: Flowchart showing the major steps in the processing of the vibrational signal. Calibration measurements allow for the current technique to account for spectral crosstalk and curvature of the spectral image.

Following calibration, data can begin to be measured. The first step is to calculate E', by solving for it in the matrix equation 2.11. As a reminder, E' is the energy of species i if no crosstalk is present. The concentration of species i can now be calculated by normalizing E' with calibration data:

$$C_i = \frac{E'_i}{\epsilon l \omega \left[\frac{\partial \sigma}{\partial \omega}\right]_i E_l} \tag{2.18}$$

Each term in this equation has been previously explained in equation 2.17. The summation of species concentrations (C_i) yields a relative total concentration (C). Referencing to a known condition in a shot to shot basis is still required to calculate an absolute total concentration. This is achieved by assuring the laser probe volume captures a known condition at every shot, such as ambient air. To this end, the jet is positioned at an off center location at either side of the probe volume so that the CCD array is able to capture both the jet and the ambient air condition on the same shot. Even though this requirement places a big restriction on the diameter of the flow to be examined, the the technique allows for absolute density measurements in non-isobaric flows where pressure is not known a priori. The variable m_v in figure 2.10 is used to denote this local normalizing vibrational multiplier. Density can now be calculated with the following equation:

$$\rho = \sum \left(X_i W_i\right) C \tag{2.19}$$

where X_i is the mole fraction of species i, W_i is the molecular weight of species i, and C is the local concentration.

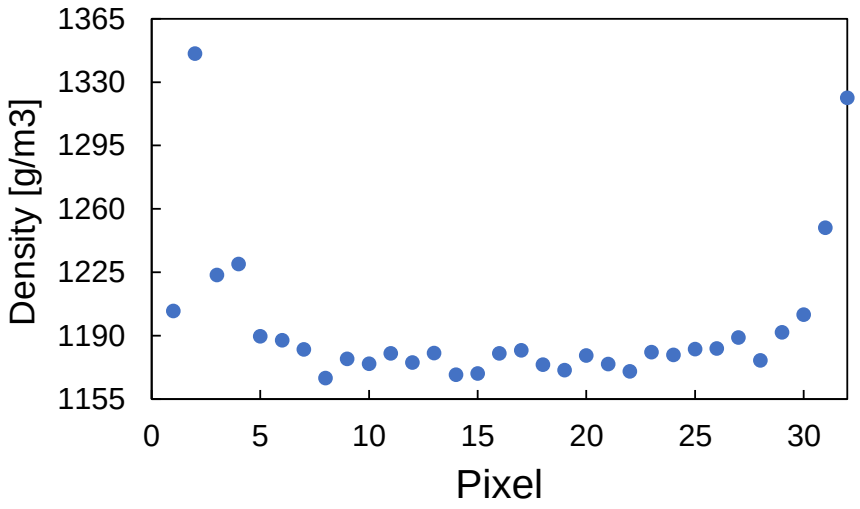

Figure 2.11: Calculated density for a set of average ambient shots.

The procedure outlined in the current section allows density to be calculated to within 1% accuracy in ambient conditions, as shown in figure 2.11. The plot shows density as a function of pixel number for a set of averaged ambient shots. As aforementioned, the changes done to the system allow to increase the effective probe volume length from about 4 mm to approximately 10.5 mm.

2.1.8 Temperature Calculation

The technique described in this paper makes use of the integral of the S-branch rotational Raman signal to calculate temperature. For the sake of illustration, a simplified harmonic oscillator model for pure rotational scattering of a single species will be used. The population at each rotational state (N_J) is derived from statistical mechanics and given by a Boltzmann distribution:

$$N_J = \frac{N g_J (2J+1) e^{-hcBJ(J+1)/kT}}{Q_{rot}} \tag{2.20}$$

$$Q_{rot} = \sum_{0}^{\infty} g_J(2J+1)e^{-hcBJ(J+1)/kT} \tag{2.21}$$

where N_J is the number density of particles in the j^{th} state of energy, N is the total number density, g_J is the degeneracy of the j^{th} state, J is the rotational quantum number, h planks constant, B is the species rotational constant, k is Boltzmann constant, T is the temperature, and Q_{rot} is the rotational partition function. The rotational Raman signal is proportional to the summation of the number density of particles over all rotational states ($\sum_0^\infty N_J$). However, as see in equation 2.20 the summation over all states recovers the partition function in the numerator. The raman signal yields, once again, a trivial explicit dependence on temperature through density, as previously seen in the vibrational section. The use of the integral method to determine temperature becomes possible only after the introduction of a filter.

As previously seen, the rotational signal for all major species (with the exception of H_2) lands very near the Rayleigh signal. A long pass filter is introduced to block the Rayleigh signal modifies equation 2.20 according to:

$$N_J = \frac{N\sum_a^\infty g_J(2J+1)e^{-hcBJ(J+1)/kT}}{Q_{rot}} \tag{2.22}$$

where "a" represents the rotational energy state corresponding to the cutoff wavelength of the long pass filter. Substituting equation 2.22 into equation 2.17 and summing over all rotational states not blocked by the filter yields the following:

$$E_{rot} = \sum_{a}^{\infty} E_{rot} \propto \sum_{a}^{\infty} N_J = \frac{N\sum_a^\infty g_J(2J+1)e^{-hcBJ(J+1)/kT}}{Q_{rot}} \tag{2.23}$$

As seen in equation 2.23, the long pass filter introduces a temperature sensitivity into the rotational Raman signal. When normalized by the local number density, the

integral becomes a function of temperature alone. As temperature increases, higher energy levels are populated. At high enough temperatures, the populated energy levels are mostly all above above the cutoff wavelength "a" of the long pass filter, as shown in figure 2.12. Consequently, the integral becomes almost constant in value and reaches an asymptote. The temperature at which the integral becomes nearly constant is considerably higher than any temperatures encountered in the present experiments and therefore should not pose an issue on the technique.

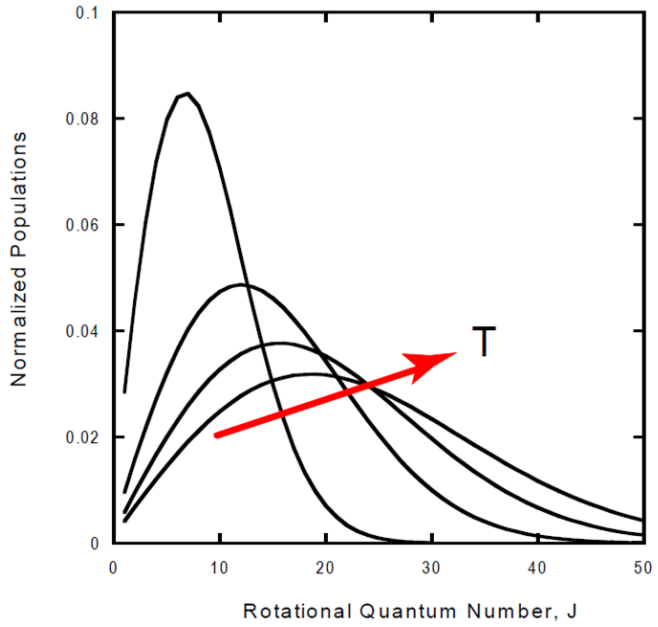

Figure 2.12: Normalized rotation populations for various temperatures. Population shifts toward greater energy states as temperature is increased. Introduction of a filter makes the integral of this population a function of temperature alone

Spectra was synthetically modeled using RAman Spectra Efficient Simulation (RAMSES) program [35]. The RAMSES version utilized for the current work does not contain rotational contributions from water or carbon dioxide. However, this

should have a negligible effect on the temperature calculation since both of this species do not significantly contribute to the rotational signal. The rotational differential scattering cross section of water is approximately two orders smaller than that of nitrogen [36], while the small rotational constant for carbon dioxide makes causes its rotational signal to land very near the laser wavelength (532 nm). The long pass filter, which has a cutoff at approximately 534.5 nm, blocks most of this signal. The symmetry of the methane molecule makes this species rotationally Raman inactive. As a result, only rotational Raman contributions from N_2, O_2, CO_2, and H_2 were considered.

The synthetic RAMSES spectra is modified to match the specifications of the spectrometer [12]. The specifications of the long pass filter is used to block signal below a certain wavelength. Furthermore, individual spectral transitions are convolved with the laser profile. Doppler and pressure broadening are not considered since their linewidth is small compared to the thickness of the laser. It has been shown that for N_2 at one atmosphere and 300K, the linewidth FWHM due to pressure and Doppler broadening is equal to 0.03 cm^{-1} [37]. The FWHM of the laser, on the other hand, is equal to approximately 144 µm, or 127 cm^{-1}. It is important to note that even though the vertical axis in the detector represents the spectral axis, the use of a slit with a finite width results in the convolution of the Raman signal with the laser profile. Therefore, it is safe to assume that broadening of the spectrum is a result of the laser width alone.

2.1.8.1 Rotational Processing

The calculation of temperature through the use of the Stokes rotational spectra is outlined in figure 2.13 and described in what follows. As aforementioned, the technique utilized in the current project exploits the temperature sensitivity of the integral of the rotational profile that is introduced by the use of a long pass filter. Experimentally, the final goal is to arrive at the following term:

$$m_R \frac{I/C}{I/C\Big|_{amb}} \tag{2.24}$$

where m_R is the local normalizing rotational multiplier, I is the integral of the rotational profile, C is the local normalized concentration, and the subscript amb stands for ambient conditions.

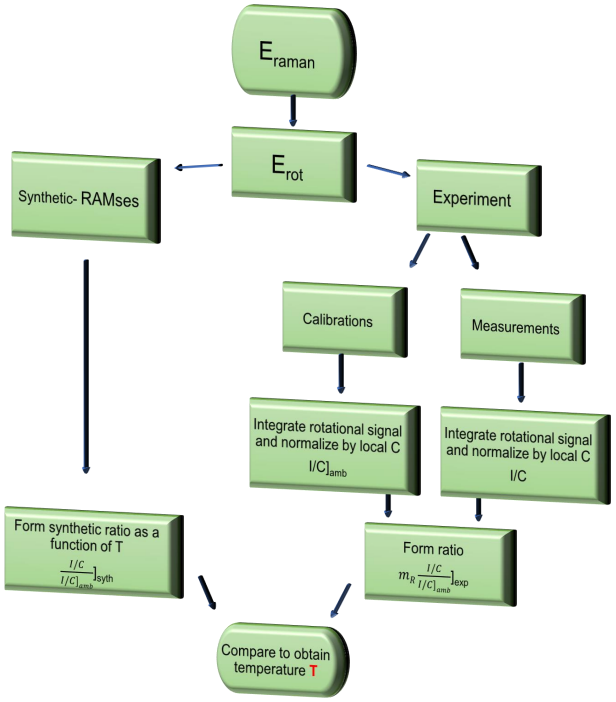

Figure 2.13: Flowchart displaying the major steps in the processing of the rotational signal. The use of a long pass filter introduced a temperature sensitivity integral of the rotational profile. Absolute temperature is calculated by comparing experimental and synthetic rotational spectra.

Calibration data is first examined to extract the rotational slit, i.e. the behavior of the rotational signal in the spatial axis. This is the term denoted as $I/C]_{amb}$ in equation 2.24. The rotational signal (I) is normalized by the local concentration (C) to eliminate the trivial dependence of the rotational signal on species concentration, previously shown in the equation 2.17. This ratio is then normalized by the rotational slit ($I/C]_{amb}$). Similarly to what was described in the vibrational processing section, this ratio needs to be referenced with a known side condition, and this multiplier is denoted as m_R. The resulting term, equation 2.24, is only a function of temperature and can now be compared to a synthetic ratio calculated with the use of the computer

code RAMSES to extract the local temperature of the flow.

2.2 Miniature Supersonic Burner

The burner utilized in the present experiments consists of two stages: a vitiation stage and a second stage. The vitiation stage follows concepts found in early jet engine combustors [22, 23], in which air is divided into two streams before flame holding and ignition takes place. This configuration allows for operation of the vitiation stage at equivalence ratios below the flammability limits of the mixture, which increases the possible range of vitiation temperatures and species composition within the vitiation stage.

Additional fuel is added at the second stage through the use of an injector. The injector length plays a crucial role in establishing the character of the external flame since it determines the residence time of the external fuel ($Fuel_{ext}$) inside the second stage of the burner. The external fuel exits the injector and proceeds to mix with the vitiated products. The fuel and vitiated air might fully combust inside the second stage if the fuel residence time is too long, i.e the injector length is too short. Conversely, if the injector length is too long, mixing between the fuel and the vitiated air will be considerably hindered due to the close proximity to the nozzle, where flow is rapidly accelerated to supersonic conditions. Therefore, an optimal range of injector lengths exists such that reactants are not fully consumed inside the second stage yet they are mixed well enough to promote combustion in the external stage. The injector length also determines the temperature at which the fuel ($Fuel_{ext}$) exits the injector. The injector carries fuel at an ambient temperature of approximately 300K. As the fuel travels through the injector inside the second stage, heat transfer through the injector wall from the vitiated products raise the temperature of the fuel. The longer the injector, the larger the amount of heat transfer and the higher

the temperature of the fuel at the exit of the injector. The fuel temperature plays an important role in the determination of the kinetic paths of combustion [38] and will be of interest for future work as explained in the following chapters. To this end, two injector lengths were studied in the current work: a 'short' injector measuring 5 cm and a 'long' injector measuring 10 cm.

3. CASE STUDY

3.1 Experimental Setup

Incoherent Raman spectroscopy has been utilized to measure gas state properties for many years [2]. Nevertheless, its application to supersonic reacting flows has been limited. Experiments that utilize laser diagnostics to measure flow properties in supersonic reacting flows commonly make use of optical windows to access the test section [3, 4, 5, 6], which hinder low signal techniques such as incoherent Raman. The miniaturized supersonic burner utilized in the present work produces a supersonic free jet which is optically accessible, allowing for the use of low level laser techniques. Raman spectroscopy was performed on the first structure of the underexpanded jet formed at the exit of the converging nozzle (approximately 3mm from the nozzle). Due to the close proximity to the burner outlet, it is safe to assume that species concentrations at the location of measurement are the same as the concentrations at the outlet. To validate this assumption, the damköhler number at the exit of the nozzle is utilized as a reference. Damköhler number is the ratio if the flow to chemical time scales. The value calculated is less approximately 0.001, which means reactions are suppressed.

Vibrational Raman scattering is utilized to determine the concentrations of major species: CO_2, O_2, CO, N_2, CH_4, and H_2O. The rotational Raman approach for the determination of pressure and temperature is the subject of current research and will appear in the future. Nevertheless, the vibrational spectra provided enough information to validate the computational results.

Vibrational Raman scattering is directly proportional to species concentrations and may be described through the following phenomenological formula:

$$E_i = E_o \epsilon l \Omega \sigma_i C_i \tag{3.1}$$

where E_o is the laser pulse energy, ϵ is an overall optical efficiency of the system, l is the length of the probe volume, σ is the Raman scattering cross-sections of species i, Ω is the solid angle of the detection optics, and C_i is the molar concentration of species i [2]. Species mole fractions were readily calculated from the vibrational Raman signals E_i by assuming that the optical parameters ($\epsilon l \Omega$) were species independent and utilizing standard values for the scattering cross sections (σ_i) [2].

Figure 3.1 shows typical high resolution Raman scattering images before processing. The two spectral images on the first row were obtained at the exit of the burner with an injector length of 5 cm, while the two images on the second row were obtained from a burner with an injector length of 10 cm. The vertical axis corresponds to the spectral axis, showing a wavelength range from 550 nm to 730 nm, which encompasses the vibrational Raman signals of the species of interest. The horizontal axis corresponds to the laser axis and shows the spatial extent of the measurement, which was 8 mm under a 1:1 conjugation, and a resolution of 250 µm. This number corresponds to the pixel resolution that can be calculated from the known number of hardware binned pixels forming each superpixel. Pixels are binned together in order to increase the SNR of the measurements. The spectral axis is shown in high resolution in the images for the purpose of quantifying and correcting the crosstalk between species. Spectral interference between species is caused by the close proximity of their Raman signals.

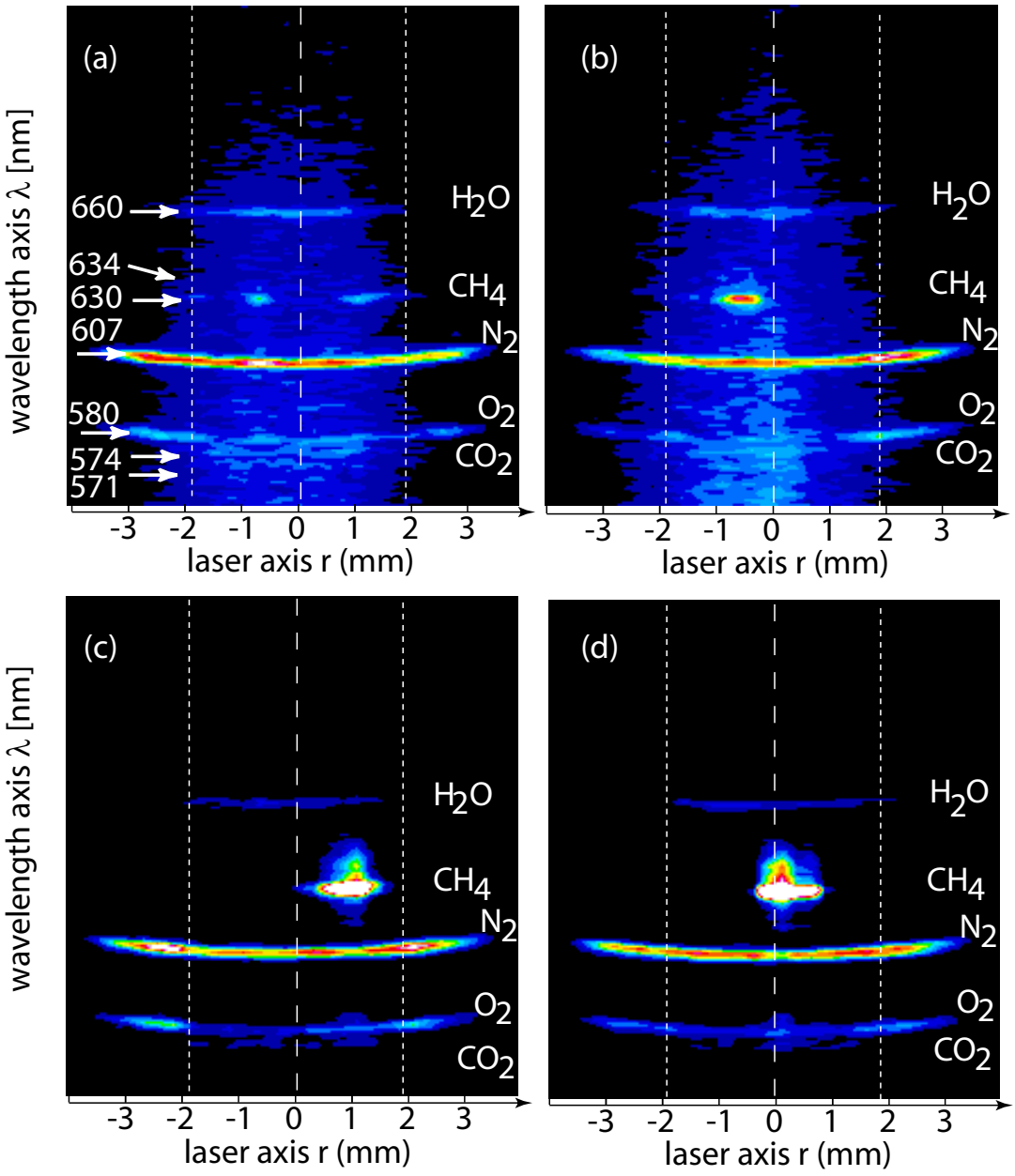

Figure 3.1: Single shot images of the vibrational Raman spectra at the outlet of the miniature burner. Figures a and b correspond to a fuel injector with a length of 5 cm. Figure c and d correspond to a fuel injector with a length of 10 cm. The center dashed line represents the center of the converging nozzle, whose diameter is approximately 3.5 mm. The two dotted lines depict the outside of the jet.

A qualitative analysis of the species Raman signals will be given in what follows, while a more quantitative approach will be presented in the results section. The intermediate species CO and H_2 are not presented in the current work due to their small concentrations. For benchmark values, the mole fractions at the exit of the nozzle were computed by performing a zero dimensional equilibrium calculation with the GRI3.0 detailed chemistry mechanism [39]. The computations yielded mole fractions of 0.5% for H_2 and 1.2% for CO, values below the noise level of the experimental measurements. Raman spectra is contained within the visible region of the spectrum, making flame chemiluminescence and soot radiation the largest sources of interference in vibrational Raman measurements. The two images corresponding to the short tube (figures 3.1a and 3.1b) show broadband interference, suggesting the presence of a luminous flame. This is not apparent in Figures 3.1c and 3.1d, suggesting a lack of a luminous flame for the long tube configuration.

The Raman signal of water, one of the main products of combustion, has a stronger signature in the short tube images than in the long tube images. The fuel (CH_4) signal, on the other hand is stronger in the images with the long tube. Examination of the Raman signals for O_2 in all four figures shows that ambient air is recovered at the outside of the jet, as evidenced by its stronger signal outside of the dotted lines. It should be noted that the experiments were performed with a burner that consists of two stages, with the first stage operated at very fuel lean conditions. Thus, the presence of O_2 in locations where there is no fuel means that the O_2 signal is caused by the presence of excess oxygen contained in the vitiated products originating from the first stage. The other main product of combustion, CO_2, is difficult to describe even qualitatively in Figures 3.1a and 3.1b due to the large interference from the flame chemiluminescence.

The Raman channel for CH_4 in all four figures shows highly intermittent behavior.

Figures 3.1a and 3.1b show a spatially intermittent fuel signal, while figures 3.1c and 3.1d show a strong asymmetrical concentration. These observations imply a lack of proper mixing inside the second stage of the burner.

The strong fuel signal, coupled with the weak signal of the products H_2O and CO_2 and general lack of chemiluminescence in Figures 3.1c and 3.1d point towards a lack of combustion for the long injector case. Conversely, the short tube results point to the direction of a flame that holds within the second stage of the burner, and produces the luminosity seen at the exit of the burner [13]. The computational results presented here, as well as the results from the experiment, will also support this conjecture.

The experimental parameters are shown in table 3.1, where $\dot{m}_{F1}$ is the vitiation fuel mass flow rate, $\dot{m}_{F2}$ is the fuel mass flow rate added through the injector in the second stage, $\dot{m}_{air}$ is the air mass flow rate, and $P_{chamber}$ is the pressure inside the second stage. The vitiation equivalence ratio (ϕ_{vit}) is calculated using the total vitiation fuel mass flow rate ($\dot{m}_{F1}$) and air mass flow rate ($\dot{m}_{air}$). The external equivalence ratio is calculated using the excess vitiation oxygen from the vitiation stage and the external fuel mass flow rate (ϕ_{ext}).

Mass flow rates in each of the lines were calculated with the aid of chocking orifices. Isentropic flow was assumed through the orifice, and mass flow rate was calculated through the use of the following formula

$$\dot{m} = \frac{A p_o \gamma}{(\gamma R T_o)^{1/2}} \left(\frac{2}{\gamma + 1} \right)^{\frac{\gamma+1}{2(\gamma-1)}} \tag{3.2}$$

where A is the area of the chocking orifice, R is the specific gas constant, T_o the total (stagnation) temperature of the gas, p_0 is the total pressure of the gas, and γ is the specific heat ratio. Chocking of the orifices was ensured by measuring pressure

upstream of the orifice.

3.2 Computational Setup

A commercial code (Fluent) is utilized to solve the Reynolds averaged form of the conservation equations for mass, momentum, and energy [40]. Turbulence is modeled through the realizable k-epsilon, where standard values were used for all the constants [41]. The Eddy Dissipation Concept (EDC) was used to represent the turbulence-chemistry interaction [42]. The EDC allows for finite-rate chemical kinetics in turbulent flow calculations. It makes use of the energy cascade model, where molecular mixing happens in the smallest of eddies or fine structures. The model assumes the fine structures contain homogeneously mixed reactants, akin to a Well Stirred Reactor (WSR), with a residence time defined as $\tau \propto (\frac{\nu}{\epsilon})^{1/2}$, where ϵ is the local dissipation rate, ν is the laminar viscosity, and C_τ is constant (here equal to 0.4082). This local flow time scale is then compared to the chemical time scales to determine which reactions will proceed and which ones will be suppressed [42, 43]. Work done by other groups has shown of this model to provide good results in flows similar to the present study [44, 41].

The EDC generally results in high computational expense due to the overhead associated with the solution of the species conservation equations. This is contrary to the conserved scalar approach, such as the flamelet modeling in all its variations which assume a pre-determined tabulated solution for chemical composition, this

Table 3.1: Experimental Parameters

Injector	$\dot{m}_{F1}$	$\dot{m}_{air}$	$\dot{m}_{F2}$	$P_{chamber}$	ϕ_{vit}	ϕ_{ext}	Re_D	Da
Short	$0.065x10^{-3}$	$2.774x10^{-3}$	0.088	2737000	0.40	0.91	66000	0.001
Long	$0.0735x10^{-3}$	$3.146x10^{-3}$	0.1	246100	0.40	0.91	72000	0.001

Units in kg/s, Pa

elimination the need for solving the species equations numerically [45, 46, 47, 48]. However, models that follow this approach rely on the fast chemistry approximation, which uncouples the chemistry from the flow solution. The complex geometry of the burner (described below) made it imperative to model a three dimensional computational domain. Unlike problems with lower dimensionality (e.g. [49]) where detailed chemistry could be modeled, the dimensionality of the present problem enforced the use of reduced chemistry. For this reason, two reduced mechanisms were considered: one consisting of two steps and one of four steps.

The Westbrook and Dryer mechanism consists of of two reactions, one of which is reversible:

$$R1' \quad CH_4 + 1.5O_2 \rightarrow CO + 2H_2O$$

$$R2' \quad CO + 0.5O_2 \leftrightharpoons CO_2$$

The two forward reactions were proposed in Dryer and Glassman 1972, who empirically derived the kinetic rates for both reactions. The backward reaction of the second step was proposed by Westbrook and Dryer 1981 to reproduce the pressure dependence of the CO oxidation. Their kinetic rates were used in this study and are shown in Table 3.2. Computational results using this mechanism are not presented in the current work since no flame-holding was achieved in either of the two injector configurations.

The Jones and Lindstedt 1988 is a four step mechanism that involves only major species. For methane oxidation, the following reactions are utilized:

$$R1 \quad CH_4 + 0.5O_2 \rightarrow CO + 2H_2$$

$$R2 \quad CH_4 + H_2O \rightarrow CO + 3H_2$$

$$R3 \quad CO + H_2O \leftrightharpoons CO_2 + H_2$$

$$R4 \quad H2 + 0.5O_2 \leftrightharpoons H_2O$$

Two different fuel oxidation paths are used to make the mechanism applicable to both premixed and coflowing diffusion flames. The familiar "water gas shift reaction", which has been shown to be important in the determination of flame structure [50], is included in this mechanism. The relatively low computational expense, the availability of explicit kinetic rate data for the reduced reaction steps, and the extensive validation this mechanism has received, made it a suitable choice for the finite rate calculations in three dimensions.

Table 3.2: Kinetic Rate Data for Westbrook and Dryer and Jones and Lidstedt Mechanisms

No.	A	β	E_a/R	Reaction Orders	Ref
R'_1	$5.03x10^{11}$	0	24056	$[CH_4]^{0.7}[O_2]^{0.8}$	[51]
R'_{2f}	$2.24x10^{12}$	0	20484	$[CO][O_2]^{0.25}[H_2O]^{0.5}$	[51]
R'_{2b}	$5x10^{8}$	0	20484	$[CO_2]$	[52]
R_1	$4.4x10^{11}$	0	15095	$[CH_4]^{0.5}[O_2]^{1.25}$	[53]
R_2	$3.00x10^{8}$	0	15095	$[CH_4][O_2]$	[53]
R_{3f}	$2.75x10^{9}$	0	10065	$[CO][H_2O]$	[53]
R_{3b}	$6.71x10^{10}$	0	13688	$[CO_2][H_2]$	[54]
R_{4f}	$5.69x10^{11}$	0	17609	$[H2][O_2]^{0.5}$	[53]
R_{4b}	$2.51x10^{14}$	0	47859	$[H_2O]$	[44]

Units in kmol, m^3, K, s, KJ.

3.2.1 Computational Domain

The governing equations were solved using a second order upwind discretization scheme. The computational domain is made up of a structured grid with approximately 1.6 million cells. It consists of a fluid domain, representing the flow inside the burner, and a solid domain, representing the outside wall and the external methane injector. The conjugate heat transfer problem was solved by specifying the external temperature of the burner from experimental data sets. A Long Wave Infrared System (LWIR) produced maps of external temperature, which were then used to generate a 2-D field that served as the CFD temperature boundary condition. Figure 3.2 shows an infrared radiation temperature map of the front side of the burner while in operation with a 5 cm injector. Two regions with a local maximum temperature can be seen in the temperature plot. The maximum temperature corresponds approximately to the plot represents the location where the vitiated flow impinges on the inside of the burner wall. Impingement regions are characterized by a higher heat transfer rate, explaining the local high temperature [55]. The second local maximum, located higher in the y-axis, can be attributed to recirculation of high temperature gas in the cavity formed between the nozzle and the external wall.

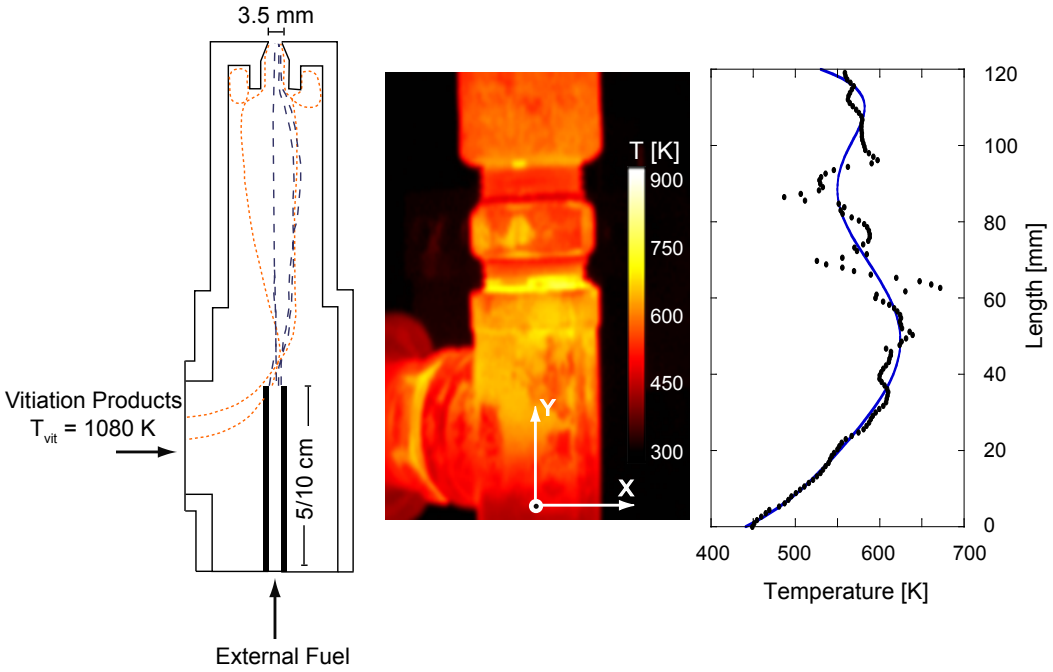

Figure 3.2: Left: 2D view of the computational domain with streamlines emanating from the vitiation stage and from the secondary methane injection. Streamlines from the vitiation stage show re-circulation regions close to the burner exit, in the cavity formed between the nozzle and the burners wall. Middle: Long wave infrared measurement showing the external temperature on the burner surface. Right: Equivalent 1D temperature profile extracted from the infrared measurement, and used as boundary conditions for the conjugate heat transfer problem. The individual dots correspond to the detailed infrared measurements, which exhibit erroneous sharp peaks due to differences in emissivity at the burner joints. The solid line used as input to the CFD was generated by a coarse filtering through the experimental data.

The spatial temperature profile for the products of the vitiation stage was the only variable that could not be explicitly measured. This is a very important parameter for the CFD since it serves as the inlet boundary condition for our domain. Preliminary computations showed little influence of the results on the form of the inlet temperature profile, and so a simple constant temperature was assumed at the inlet. An adiabatic flame temperature could not be assumed at his location due to heat loss suffered in the first stage. Instead, an iterative approach was followed to determine

the appropriate inlet temperature. Two experimental quantities were first measured: the chamber pressure and the temperature at a known location inside the second stage of the burner. The pressure was measured using pressure gauges, while the temperature was measured with a thermocouple inserted through the orifice where the secondary fuel is usually delivered. Given that the variable in question depends only on the operation of the first stage, it was not necessary to run the external fuel and have the seconds stage operating during the experiments. Computationally, the inlet temperature was modified until the chamber pressure and the temperature at the specified location matched the experimental values to within a certain tolerance. This procedure is shown in Figure 3.3.

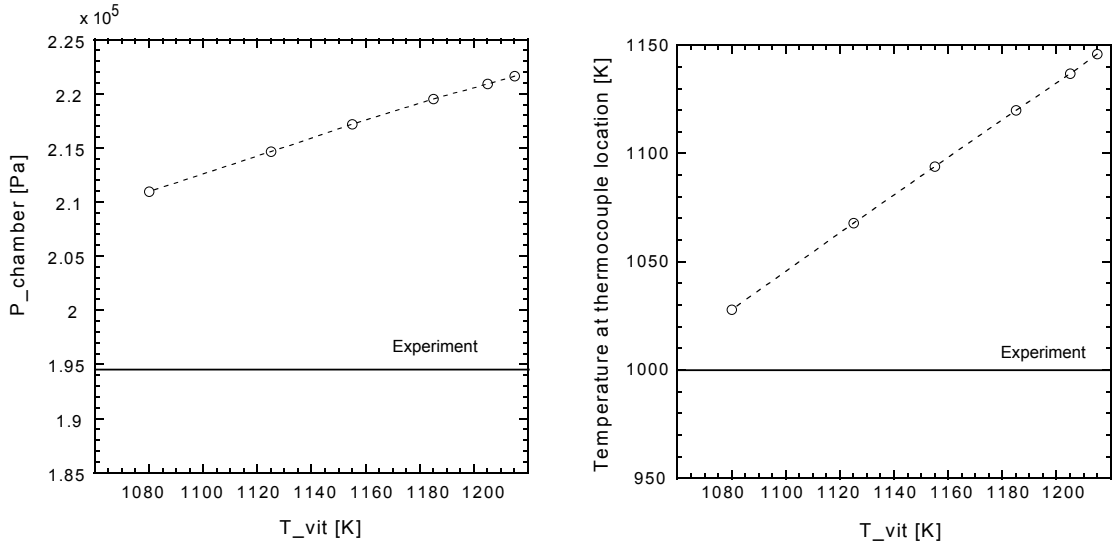

Figure 3.3: Left: Computational chamber pressure as a function of the vitiation temperature. Right: Computation temperature at specified location as a function of the vitiation temperature. The straight line represents the experimental values. The X corresponds to the vitiation temperature value assumed as input to the computations.

The left plot shows the computational chamber pressure against the vitiation temperature, while the plot on the right shows the temperature at the point of the thermocouple measurement versus the vitiation temperature. The difference in slopes in the two plots shows a greater sensitivity in the temperature. This behavior can be explained by a simple examination of the 1D equation for choked flow, which states that $\dot{m} \sim \frac{p}{\sqrt{T}}$ [56]. The value chosen for all the computations in the present study is denoted by the X, which corresponds to a vitiation temperature of 1080 K. The use of this value resulted in the computational chamber pressure differing form the experimental pressure by approximately 6%, and the computational temperature at the specified location near differing by less than 3%.

A grid independence test was performed for three different grid sizes of 1.6, 2.5, and 3.4 million cells. Area-weighted total temperature and total pressure were monitored at the outlet. Convergence for each case was determined by requiring the mass flow rate imbalance between the inlets and outlet to be less than one percent of the total mass flow rate. Additionally, pressure, temperature, and CH_4 mass fraction were monitored at the outlet until they were approximately constant in value. No significant changes were observed between the coarse, medium, and large grids. Consequently, the coarse grid is utilized for the computational modeling in the present work.

3.3 Results

3.3.1 Computational Results

Results of the temperature inside the second stage of the burner and mole fractions at the outlet for the short and long tube configurations are presented in figure 3.4. Only the mole fractions of CH_4, O_2 and H_2O are presented since they provide enough information to understand the salient features of the flow inside the second stage. The temperature contour for the short tube shows evidence of a flame attached to the fuel injector. As the flame approaches the exit nozzle, some of the high temperature fluid recirculates in the cavity formed between the external wall and the nozzle. Consequently, the heat transfer to the external wall in this area is increased. This result is corroborated by the local high temperature seen in the infrared measurements of the external wall (figure 3.2). An asymmetrical distribution of the flame in space is seen as it reaches burner exit. The temperature map for the long tube, on the other hand, does not show any combustion. It is very clear by the comparison of the two cases that a non-premixed flame is attached at the tip of the injector tube, provided that the vitiated air for the first stage can sufficiently mix with the preheated external fuel. This will be corroborated by the experimental results that follow.

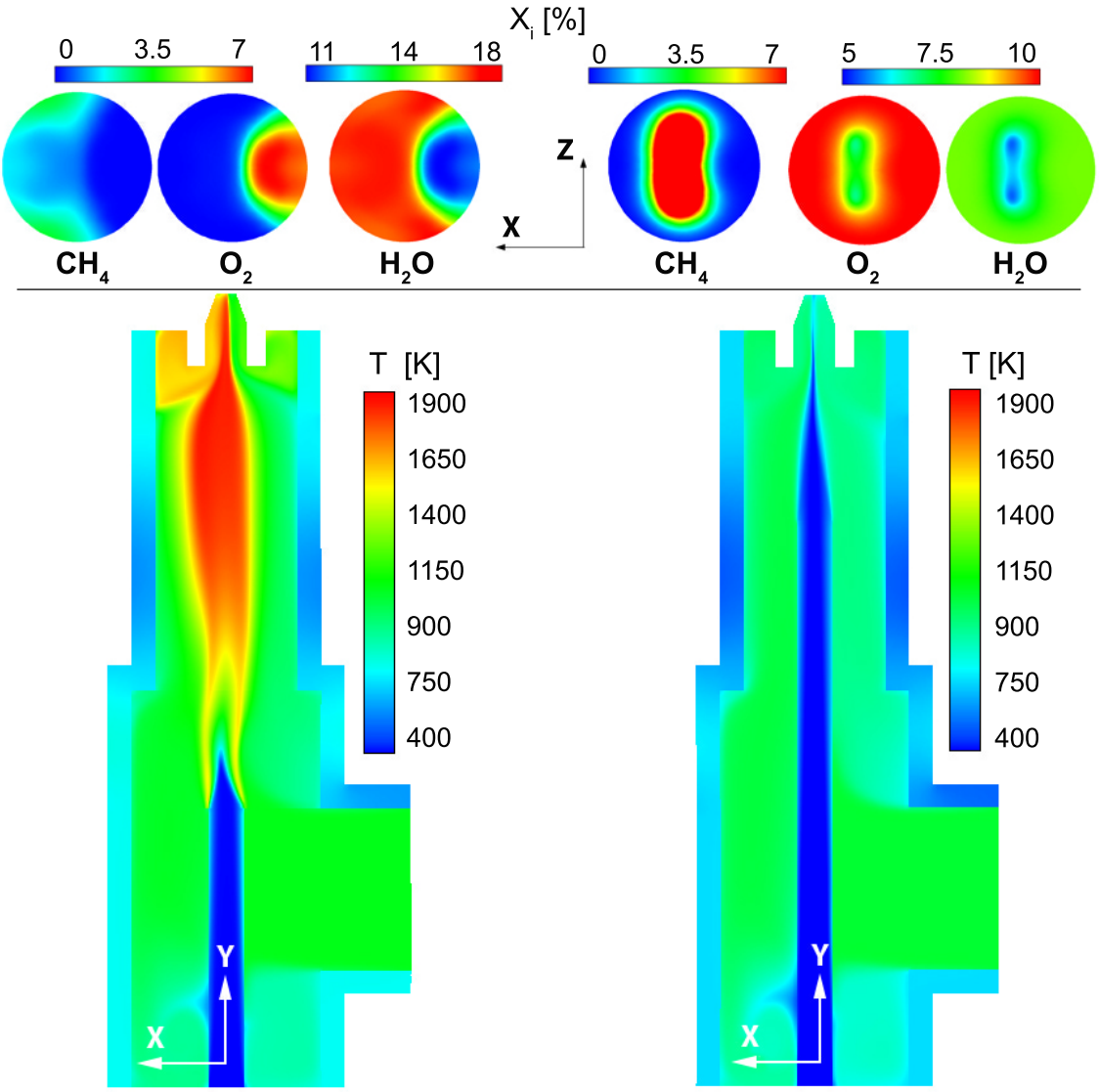

Figure 3.4: Favre averaged temperature contours of the second stage of the burner and mole fraction distributions at the outlet. Figure on the left corresponds to a burner with a 5 cm fuel injector, while the figure on the right corresponds to a burner with a 10 cm fuel injector. Favre averaged mole fractions shown at the exit plane of the nozzle are expressed as percentages

Examination of the fuel mole fraction (CH_4) at the outlet of the short tube

configuration displays an uneven distribution in space. The lack of CH_4 on the right part of the outlet could denote either a full consumption of fuel in this region or simply a lack of fuel due to improper mixing. If complete fuel consumption was the cause for this observation, we would expect an increase in the combustion products and a depletion of the oxidizer on the right side of the outlet. However, the small water mole fractions and the large mole fraction of the oxidizer (O_2) on the right side of the outlet both suggest that the lack of fuel is caused by improper mixing. The mole fraction distributions, in combination with the temperature asymmetry near the outlet of the nozzle, show combustion taking place only on the left side. These results qualitatively agree with the experimental results shown in Figures 3.1a and 3.1b , which also show an intermittent behavior of methane in space. The intermittency displayed in the single-shot experiments is a result of turbulence inside the second stage. Since only the Favre averaged solution of T and X_i were computed, results of the intermittent behavior in time are not available in the CFD.

The mole fractions for the long tube configuration show a strong concentration of CH_4 at the center of the outlet. This is consistent with the experimental results shown in Figures 3.1c and 3.1d. The high concentration of fuel at the center decreases the mole fractions of the rest of the species in this region and increases them elsewhere. Similarly to the short tube computation, results show non uniform mixing between vitiated products and external fuel.

3.3.1.1 Residence Time Distribution

The Residence Time Distribution (RTD) of the external fuel is used to characterize the amount of mixing inside the second stage of the miniature combustor. The RTD is commonly obtained by injecting a tracer with either a pulse or step input and

then measuring its concentration at a monitoring location [57]. In the present work, the step method was chosen in order to avoid any round off errors due to the small external fuel concentration. For a step input, the concentration at the monitoring location yields the cumulative distribution function, or F curve [58]. This curve is the differentiated to obtain the RTD curve (E(t)).

The residence time of interest in the current work corresponds to the time a fluid fuel element spends inside the second stage of the burner after exiting the injector. The time inside the injector is not relevant since no mixing is taking place. For this reason, two locations to monitor the CH_4 concentration were chosen: one at the end of the injector and one at the outlet. The RTD of each monitor is shown in figure 3.5 for both, the short and long injector case.

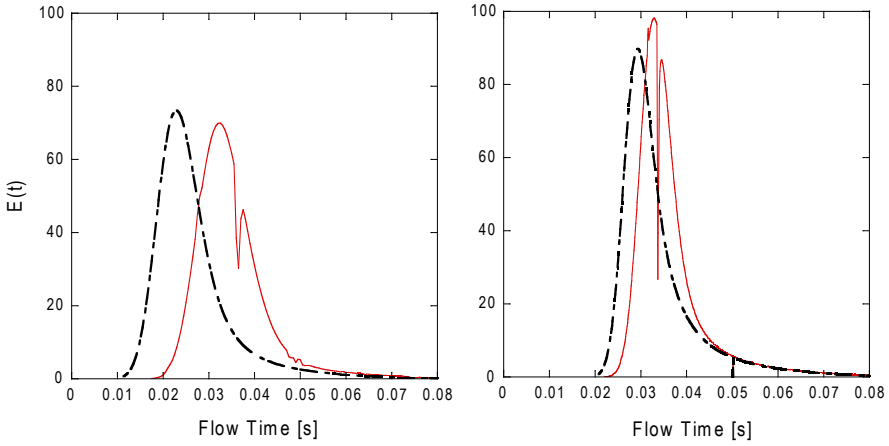

Figure 3.5: Residence time distribution of the methane particles inside the computational domain. The graph on the left corresponds to a 5 cm methane injector while the one of the right to an 10 cm methane injector. Each graph contains two curves; one of them represents the time methane particles take to travel from the secondary methane inlet to the end of the injector while the other the time to reach from the inlet to the outlet.

Several statistical parameters of the RTD functions were used to determine the level of mixing and combustion inside the second stage: the mean residence time (t_m), the variance (σ^2), and the Coefficient Of Variation (COV) [58]. They were calculated as follows:

$$t_m = \int_0^\infty tE(t)dt, \tag{3.3}$$

$$\sigma^2 = \int_0^\infty (t - t_m)^2 E(t)dt, \tag{3.4}$$

$$COV = \frac{\sigma^2}{t_m} \tag{3.5}$$

The mean residence time represents the average time a particle spends between the inlet and the monitor. The average time between the inlet and the end of the injector is denoted as t_{inj}, while the average time between the inlet and the outlet is denoted as t_{outlet}. The mean residence time in the region of interest is given by $t_m = t_{outlet} - t_{inj}$. The variance measures the spread of the distribution and is given by the second moment of the RTD while the COV measures the relative spread. A system with a good mixing quality would have a COV value close to zero. For instance, in the extreme case of a plug-flow simulation, the COV value is zero since all the elements have the same residence time ($\sigma^2 = 0$). The values of these statistical parameters are shown in Table 3.3.

Table 3.3: Residence Time Distribution Statistical Parameters

Case	t_{inj}	t_{outlet}	t_m	σ^2	COV
Short Injector	0.0266	0.0376	0.0110	0.001	0.0915
Long Injector	0.0338	0.0373	0.0035	$5.31x10^{-4}$	0.1529

Units in s.

The mean residence time (t_m) and the variance (σ^2) offer insufficient information about the quality of mixing when analyzed independently. For instance, the σ^2 for the long injector case is about two times smaller than the σ^2 for the short injector case. This does not mean that the long injector configuration provides better mixing. As evidenced by CH_4 mole fraction distribution in figure 3.4, it simply means that the fuel particles traveled a direct path to the outlet without enough time to diffuse with the products of vitiation. The COV is a more powerful variable since it also contains information regarding the mean residence time. The short injector case has the smaller COV value, denoting a better mixing of the external fuel with the vitiation products. The improved mixing is a result of a shorter length of the injector, since it extends the fuel residence time. The COV value of 0.0915 is small enough to ignite the mixture. However, it is not small enough to evenly mix the mixture, as seen by the intermittentcy of the species in space in figure 3.4.

3.3.2 Experimental and Computational Results

To set up a meaningful comparison between the CFD results and the experimentally collected statistics in the form of distribution functions, we must first recognize and correct a significant bias between the two approaches. Figure 3.6 shows the geometry of the experimental laser probe superpixels with a rectangular shape and

equal areas ($S_i = a \times b$). For each rectangle, a=b=250 µm in the particular experimental setup.

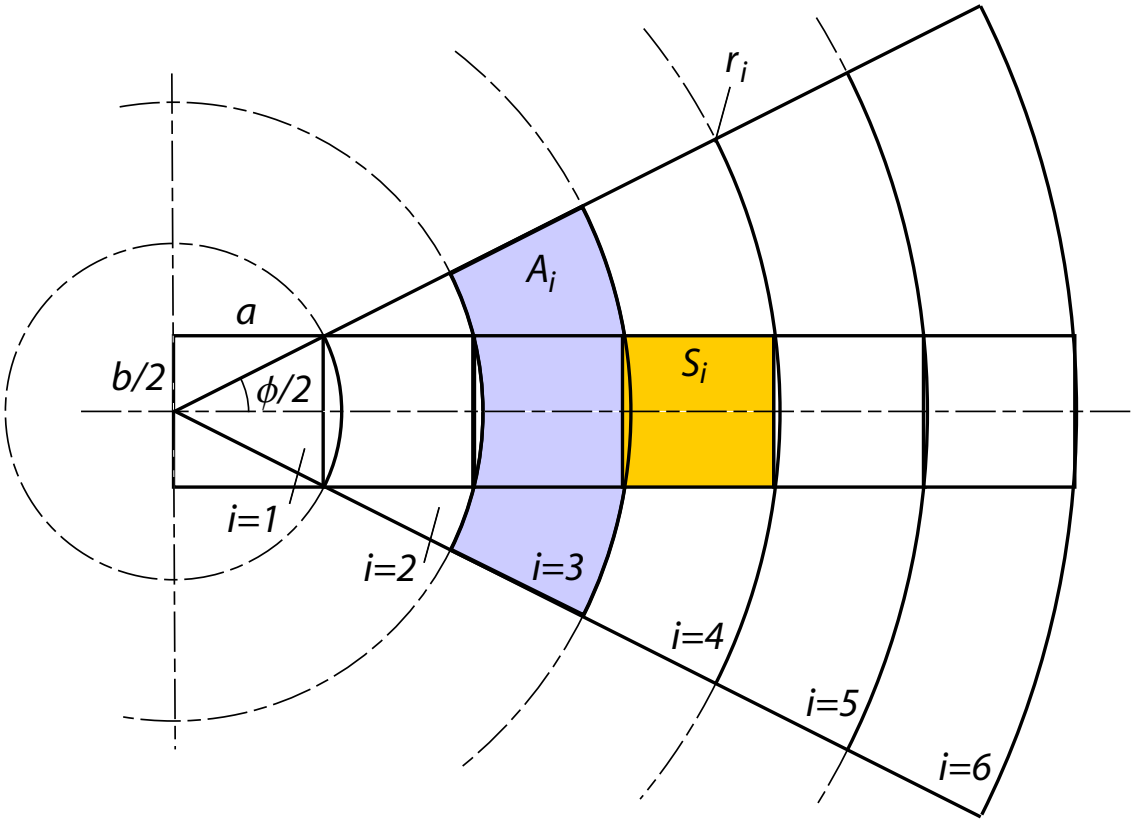

Figure 3.6: Geometrical difference between laser probe superpixels and CFD cells results in bias for the collected statistics. Rectangular laser probe area $S_i = a \times b$ does not depend on superpixel number (i) while wedge CFD cell area A_i increases drastically with radial location (r_i) or cell number (i).

The equal superpixel area implies an uniform probability of collection for a measurement anywhere across the jet exit. At the same time, the CFD results are generated in grid cells with cylindrical symmetry, and a wedge-like form factor, as shown in figure 3.6. The cell area (A_i) depends strongly on the location of the cell,

expressed as radius (r_i) or cell location (i). When examining the statistics generated by the CFD, like the ones shown at the jet exit in figure 3.7, it is important to note that thermochemical conditions at the periphery are going to be collected with higher frequency, and this bias becomes stronger as radius r_i increases. The area ratio A_i/S_i becomes a weight factor that converts the measurement PDFs to those generated by the CFD results. Using an approximation for the radial location ($r_i \approx i \times a$) and the calculated included angle for the CFD cells ($\phi = 0.93rad$) we may evaluate the weight factors as

$$w_i \equiv \frac{A_i}{S_i} \approx \frac{(\phi/2\pi)\pi r_i^2 - (\phi/2\pi)\pi r_{i-1}^2}{a^2} = \phi(2i-1)/2.$$

The result is a simple linear relationship of area ratio with respect to radial position, corresponding to the Jacobian of transformation between a Cartesian frame of reference for the measurement and the axisymmetric frame of reference of the CFD.

Figure 3.7 compares experimental and numerical species mole fractions at the exit of the burner with the short tube configuration. Results for the reactants mole fractions (CH_4 and O_2) show the best agreement. Both the experiment and the computation show high counts at small mole fractions, suggesting combustion took place inside the burner. The experimental and numerical agreement of the main products of combustion, H_2O and CO_2, on the other hand, do not show as good as an an agreement. The consumption of reactants, the increase in mole fractions of CO_2 an H_2O, and the presence of broadband luminosity in the spectral images, all signify that combustion is taking place inside the second stage of the burner for the short tube configuration. Both CFD and experiments point to the presence of a non-premixed flame attached at the injector tip.

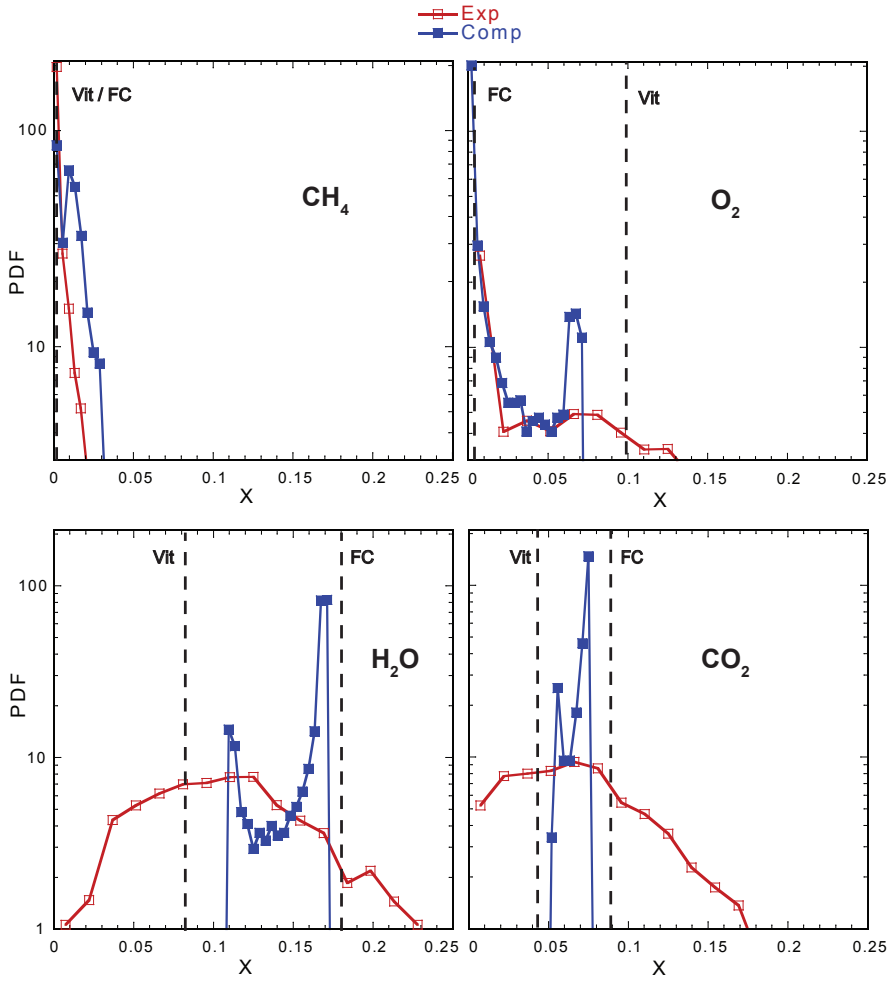

Figure 3.7: Experimental and computational comparison of the PDF of the mole fraction distribution for a short injector configuration. Noticeable large spread in the experimental results hinder the comparison to CFD. Flame chemuluminesccenec is the main source of noise in these measuremtns.

Examination of the results for the long tube configuration in Figure 3.8 show better comparison between experiments and computations than the ones for the short tube configuration. The mole fraction PDFs of CH_4 and CO_2 show the best agreement. The experimental values for O_2 an H_2O are over and under-predicted, respectively, in relation to the computational values. This discrepancy is most likely

caused by experimental errors in the conversion from Raman scattering to species mole fractions. Even if the results lack quantitative accuracy, their qualitative interpretations should still be valid. Lack of combustion for the long tube configuration is signified by the lack of flame luminosity in the spectral images, the lack of oxidizer consumption, and small mole fractions for the main combustion products.

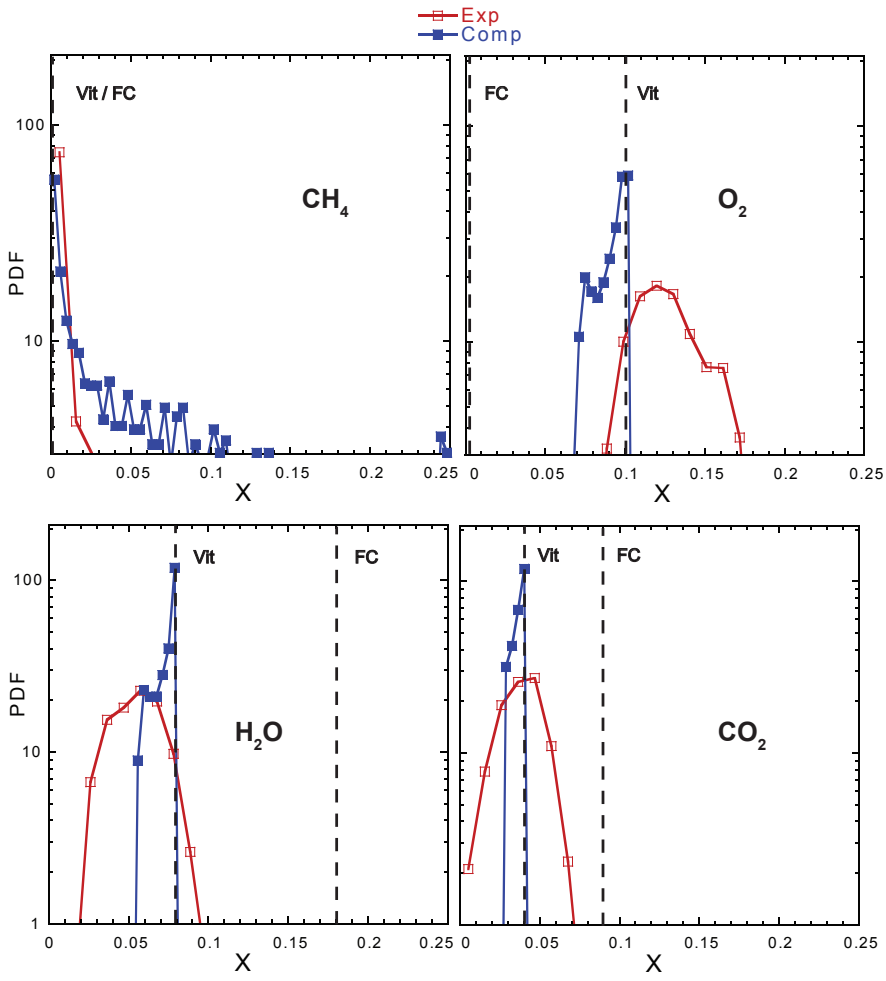

Figure 3.8: Experimental and computational comparison of the PDF of the mole fraction distribution for a long injector configuration. The spread in the experimental data is considerably less than the one shown for the short injector, attributed to the lack of a flame.

A bimodal behavior can be observed in the computational results for both short and long injector configurations. This behavior can be understood by examination of figure 3.9, which shows the mole fraction distribution and reaction rates for CH_4, CO_2, and H_2O along the symmetry plane of the burner. The reaction rate for the fuel shows that most combustion takes place in the triple flame attached to the injector. However, some of the fuel manages to escape this flame and recirculates in the left cavity formed between the nozzle and the external wall, as evidenced by the CH_4 mole fraction distribution. This fuel mixes with the vitiated air and ignites, causing flame holding at a second location. This result is consistent with the experimental Infrared temperature measurements of the external walls of the burner, which showed an additional local temperature maxima in the same region (figure 3.2). The mole fraction composition of this stream is very similar to the composition from the combustion of the attached flame and together, they correspond to the largest peak seen in the mole fraction PDFs in figure 3.7. The second mode observed in the mole fraction PDFs originates re-circulation zone formed between the nozzle and the burners wall located on the right side. As shown in figure 3.9, mole fractions for the main products of combustion, CO_2 and H_2O, increase in this region. Examination of the reaction rates for the three species displayed show no reaction taking place at this location. Instead, a portion of the combustion products from one of the flames gets entrained into the cavity as a result of the three dimensionality of the flow. It then it mixes with the vitiated products, increasing the mole fractions for CO_2 and H_2O and lowering the mole fraction for O_2. Results like this provide comfort in the initial decision of going for the full flow dimensionality at the cost of a more detailed chemical approach.

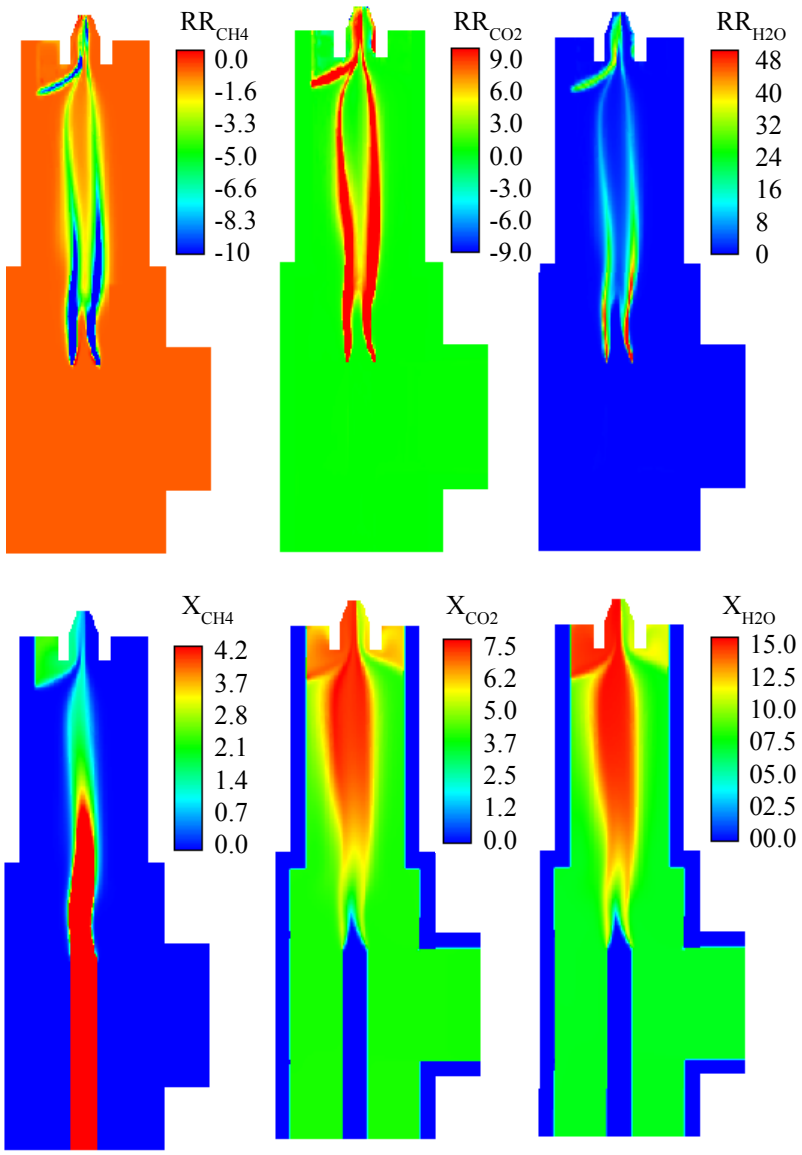

Figure 3.9: Contour plots for the reaction rates and mole fractions for the fuel and two main products of combustion symmetry plane taken at the symmetry plane. Reactions are observed is observed at two locations: at the tip of the fuel injector and at the recirculation zone formed in the cavity between the nozzle and the wall of the burner.

For comparison, two mole fraction values were plotted using dashed lines in figures 3.7 and 3.8, one denoting the theoretical full consumption of the reactants (FC) using

equilibrium calculations and another one corresponding the mole fractions from the vitiation stage (Vit). The vitiation values would denote the case when the vitiation products do not mix with the additional fuel and maintain its composition. As seen in figure 3.7, the agreement between the theoretical values and the computational results is not exact. This discrepancy is readily explained by the flow behavior in the re-circulation regions formed between the nozzle and the external wall of the burner. For instance, both CO_2 and H_2O show the largest peak at a smaller mole fraction that the theoretical full consumption value (FC), while the second peak to be at at a mole fraction value larger than the non-mixing scenario (Vit). When some of the products of combustion are entrained into the re-circulation zone on the top right of the burner the values for the products of combustion, CO_2 and H_2O, increase on the right hand side of the burner, shifting the smaller peak to the right. The peaks corresponding to a full consumption have to decrease accordingly. A shift in the mole fraction is seen as opposed to broadening due to the fact that the re-circulation zone allows for a excellent mixing to take place. The opposite is true for oxygen. When products of combustion are entrained into the right cavity, the vitiated oxygen is diluted, resulting in a mole fraction smaller than the vitiated value.

The bimodal behavior is not as visible in the experimental results, which has a broader range of mole fraction values. As seen in Figure 3.1 flame luminosity is the main source of noise in the short tube configuration, and in some shots it overcomes the signal levels. When this occurs the mole fraction values for some species, after background subtraction, are artificially inflated or deflated. More importantly, the computational results show Favre-averaged mole fraction distributions, while the PDF for experimental results do not discriminate between averages and fluctuations. The greater the fluctuations, the larger the spread in the experimental data. Nevertheless, the average values in the experiments and computations show similar

behavior.

4. FUTURE WORK

MILD (Moderate or Intense Low oxygen Dilution) combustion has received increased attention for its reduction in pollutant emission [59]. A volumetric reaction limits the amount of thermal gradients, thus avoiding potential hot sports [60]. Lowering the final combustion temperature limits the production of thermal NOx. MILD combustion is of particular interest for future work of the present research group due to its flameless oxidation. As previously described, flame luminosity is the largest source of noise in the experiments. Achieving combustion while suppressing the flame would considerably increase the SRN.

A transition to this type of combustion is possible by meeting the following criteria: an oxidizer temperature that is higher than the self-ignition temperature of the mixture, a large reactant dilution, and high turbulence. The two stage configuration of the burner makes it possible for the first two criterion to be met. The fuel lean vitiation stage pre-heats the oxidizer prior to entering the second stage of the burner, and additionally dilutes the oxidizer with products of combustion.

The fuel injector in the second stage determines if the third criteria is met. An environment with high turbulence is desired to decrease the mixing time scales. This allows for reactions to proceed in a diffuse region and approach conditions similar to a well-stirred reactor. As evidenced by both computational and experimental results, mixing of the fuel with the oxidizer is considerably hindered by the current configuration. The delivery of additional fuel has to be modified either by increasing the exit velocity of the fuel, which increases entrainment for better mixing, or by changing the co-flowing configuration. Preliminary experiments with these suggestions applied have shown promise in reducing intermittency of the burning.

The temperature of the fuel exciting the injector is also of concern. For a short injector configuration, this temperature is on average 500K. The high fuel temperature and relatively low exit velocity allows for flameholding to occur at the tip of the injector. Figure 4.1 displays the temperature distribution as a function of height in the second stage.

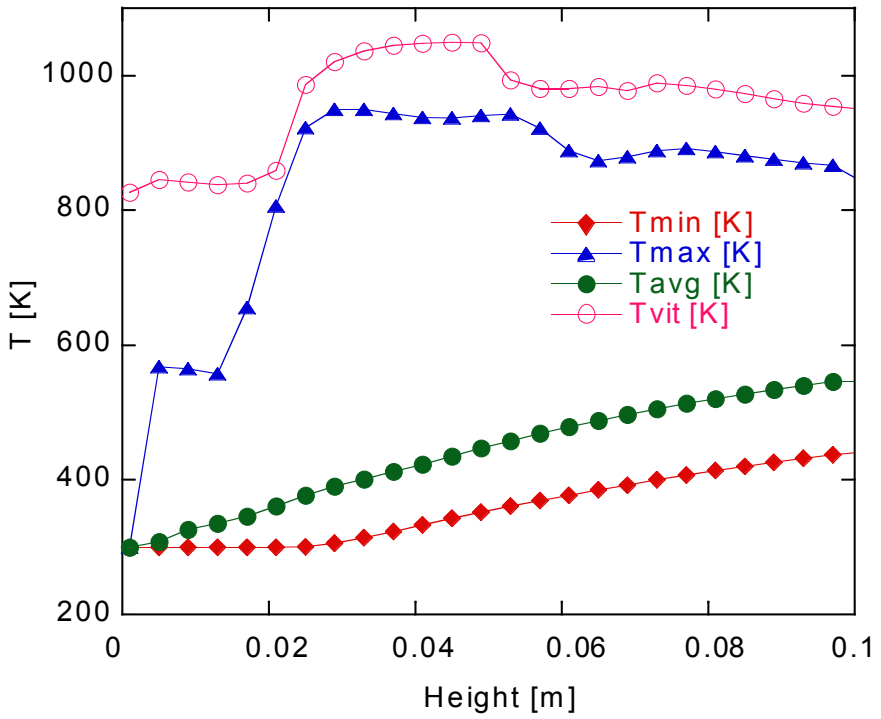

Figure 4.1: T_{avg}, T_{min}, and T_{max} show the average, minimum, and maximum temperatures, respectively, of the fuel inside the injector at different y locations. T_{vit} is the average temperature of the vitiation products.

The external methane enters the injector at 300 K and increases its temperature as a result of the heat transfer from the vitiated products. Three temperatures (T_{avg}, T_{min}, T_{max}) describe the behavior of the fluid inside the injector, while T_{vit} describes

the behavior of the products of vitiation. At a height of about 2.5 cm, the products of vitiation impinge upon the injector wall. This region undergoes the highest rate of heat transfer, as seen by the sharp increase in heat transfer in figure 4.2.

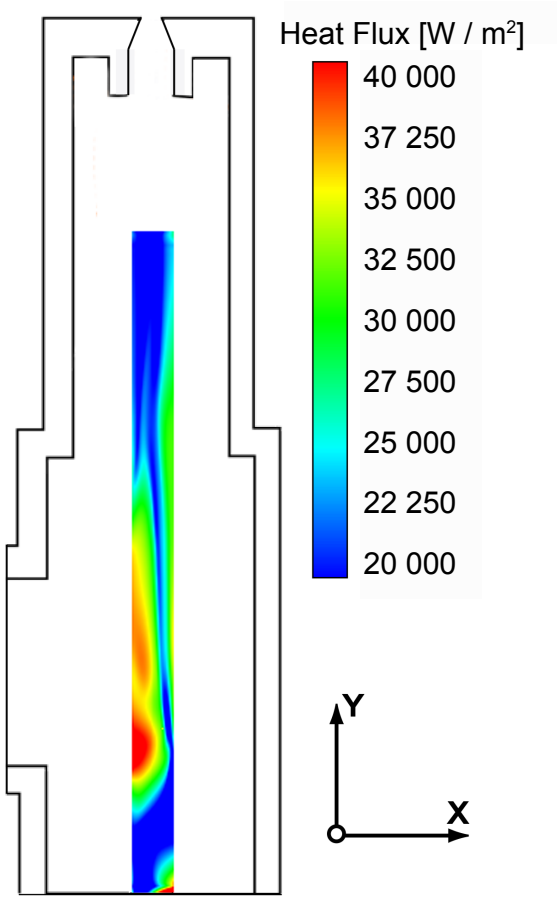

Figure 4.2: Heat flux contour for long injector configuration. Highest heat flux is seen at the region where the vitiation products impinge on the injector.

Figure 4.2 also shows the two heat transfer mechanisms at different heights of the injector. Heat transfer in the first 5 cm of the injector is mainly a result of the vitiated flow impinging on the injector wall. Further along though, the vitiated products and the external fuel move in a co-flowing configuration. Furthermore, the temperature

of the vitiated products (T_{vit}) decreases due to heat loss to the surroundings and to the injector. As a result, heat transfer to the injector is reduced and the temperature of the external fuel does not increase as rapidly as it did along the first segment.

Figures 4.1 and 4.2 demonstrate that the injector configuration needs to be altered to minimize heat transfer to the fuel. This could be done in two ways: by replacing the material of the injector to one with lower thermal conductivity, such as a ceramic, or changing the location of the injector to be further upstream.

5. CONCLUSIONS

The primary research objective of this study was to advance our understanding of flame suppression in supersonic flows by improving a technique capable of measuring the full thermochemistry in such non-isobaric reacting flows. This was achieved through two different channels: firstly, by further developing an incoherent Raman laser diagnostic technique capable of independently measuring temperature and density, and secondly, by analyzing and modifying an existing miniature supersonic burner (currently utilized as the test bed for the experiments). Several steps were taken with the final goal of improving the SNR of the system.

- **Spectral crosstalk and species sensitivity**: A systematic calibration procedure was developed to account for crosstalk in measurements. Crosstalk is a result of spectral overlap and image curvature. The calibration procedure developed in this work also allowed for the use of individual species slit functions in the processing of data. Species sensitivity in the array was shown to introduce significant error, as shown by Figure 2.7. These two improvements increased the effective length of the probe volume from 4 mm to approximately 10 mm.

- **System timing and energy normalization**: The experimental setup was improved by introducing a reliable energy normalization system, consisting of a photodiode, photodiode amplifier, and boxcar averager. Furthermore, the timing of the experimental setup was modified by introducing a pulse generator. The pulse generator allowed for the syncing of the CCD exposure time with the laser pulse. The new system was shown to increase SNR values by up to 20%.

- **Modification of density and temperature calculation**: Improvements to the processing of the vibrational and rotational spectra were made. These included side normalization to known conditions as well as individual slit functions.

- **Case study**: Performed CFD on the inside of miniaturized burner. Results showed a lack of proper mixing. More importantly, they provided a better understanding into the steps that need to be taken in order to transition the burner to the MILD regime. Figures 4.1 and 3.4 show that the fuel injector configuration needs to be modified in order to increase mixing and minimize fuel pre-heating. These two steps will likely transition the combustion mode inside the second stage of the burner into the MILD regime. MILD combustion is desired due to its flameless characteristics, which would facilitate measurements in reacting flows using the laser diagnostic technique presented herein.

REFERENCES

[1] C. R. McClinton, "X-43 scramjet power breaks the hypersonic barrier," 44th AIAA Aerospace Sciences Meeting and Exhibit, vol. 44, pp. 1–10, 2006.

[2] A. C. Eckbreth, Laser Diagnostics for Combustion Temperature and Species. Cambridge, MA: Abacus Press, 1988.

[3] T. J. Anderson and A. C. Eckbreth, "Simultaneous coherent anti-Stokes Raman spectroscopy measurements in hydrogen-fueled supersonic combustion," Journal of Propulsion, vol. 8, pp. 7–15, January 1992.

[4] A. Cutler, P. Danehy, R. Springer, S. O'Byrne, D. Capriotti, and R. DeLoach, "Coherent anti-Stokes Raman spectroscopic thermometry in a supersonic combustor," AIAA Journal, vol. 41, pp. 2451–2459, 2003.

[5] S. O'Byrne, P. M. Danehy, S. A. Tedder, and A. D. Cutler, "Dual-pump coherent anti-Stokes Raman scattering measurements in a supersonic combustor," AIAA Journal, vol. 45, pp. 922–933, April 2007.

[6] D. J. Micka and J. F. Driscoll, "Combustion characteristics of a dual-mode scramjet combustor with cavity flameholder," Proc. Combust. Inst., vol. 32, pp. 2397–2404, 2009.

[7] R. S. Barlow, C. D. Carter, and R. W. Pitz, Applied Combustion Diagnostics. New York: Taylor and Francis, 2002.

[8] P. A. Nooren, M. Versluis, T. H. van deer Meer, R. S. Barlow, and J. H. Frank, "Raman-Rayleigh-LIF measurements of temperature and species concentration in the delft piloted turbulent jet diffusion flame," Applied Physics B, vol. 71, pp. 95–111, 2000.

[9] V. Bergmann, W. Meier, D. Wolff, and W.Stricker, "Application of spontaneous Raman and Rayleigh scattering and 2D LIF for the characterization of a turbulent CH4/H2/N2 jet diffusion flame," Applied Physics B, vol. 66, pp. 489–502, 1998.

[10] D. Geyer, 1D Raman/Rayleigh experiments in a turbulent opposed-jet. PhD thesis, Technical University of Darmstadt, 2005.

[11] F. Fuest, R. S. Barlow, D. Geyer, F. Seffrin, and A. Dreizler, "A hybrid method for data evaluation in 1D Raman spectroscopy," Proceedings of the Combustion Institute, vol. 33, pp. 815–822, 2011.

[12] A. Bayeh, Rotational and vibration Raman spectroscopy for thermochemistry measurements in supersonic flames. PhD thesis, Texas A&M University, 2013.

[13] A. C. Bayeh, D. W. Ellis, and A. N. Karpetis, "Miniaturized combustor for supersonic methane-air flames," Journal of Propulsion and Power, vol. 30:5, pp. 1167–1174, 2014.

[14] J. Kojima and Q. V. Nguyen, "Laser pulse-stretching with multiple optical ring cavities," Applied Optics, vol. 41, pp. 6360–6370, October 2002.

[15] R. S. Barlow and P. C. Miles, "A shutter based line-imaging system for single-shot Raman scattering measurements of gradients in mixture fraction," Proceedings of the Combustion Institute, vol. 28, pp. 269–27, 2000.

[16] A. N. Karpetis and R. S. Barlow, "Measurements of scalar dissipation in a turbulent piloted methane/air jet flame," Proceedings of the Combustion Institute, vol. 29, pp. 1923–1936, 2002.

[17] D. E. Battey, J. B. Slater, R. Wludyka, H. Owen, D. M. Pallister, and M. D. Morris, "Axial transmissive f/1.8 imaging Raman spectrograph with volume-

phase holographic filter and grating," Applied Spectroscopy, vol. 47, pp. 1912–1919, 1993.

[18] R. Barlow, G.-H. Wang, P. Anselmo-Filho, M. Sweeney, and S. Hochgreb, "Application of Raman/Rayleigh/LIF diagnostics in turbulent stratified flames," Proceedings of the Combustion Institute, vol. 32, pp. 945–953, 2008.

[19] H. Owen, D. Battey, M. Pelletier, and J. Slater, "New spectroscopic instrument based on volume holographic optical elements," Proceedings SPIE, vol. 2406, pp. 260–267, 1995.

[20] M. Lequime, "Tunable thin-film filters: review and perspectives," Proceedings of The Society of Photo-Optical Instumentation Engineers, vol. 5250, pp. 302–311, 2003.

[21] G. Chartier, Introduction to Optics. New York: Springer, 2005.

[22] A. H. Lefebvre, Gas Turbine Combustion. Washington: Hemisphere Publishing Company, 1983.

[23] A. H. Lefebvre, "The role of fuel preparation in low-emission combustion," Journal of Engineering for Gas Turbines and Power, vol. 117:4, pp. 617–654, 1995.

[24] P. Wu, N. Nelson, and Y. Tseng, "A general method for improving spatial resolution by optimization of electron multiplication in CCD imaging," Optics Express, vol. 18, pp. 5199–5212, 2010.

[25] K. Sperlich and H. Stolz, "Quantum efficiency measurements of EMCCD cameras: high spectral resolution and temperature dependence," Measurement Science and Technology, vol. 25, pp. 1–10, 2014.

[26] N. Smith, C. Coates, A. Giltinan, J. Howard, A. O. Connor, and S. O'Driscoll, "EMCCD technology and its impact on rapid low-light photometry," Proceedings of SPIE, vol. 5499, pp. 162–171, 2004.

[27] R. L. McCreery, Raman Spectroscopy for Chemical Analysis. New York, NY: John Wiley and Sons, 2000.

[28] P. C. Miles and R. S. Barlow, "A fast mechanical shutter for spectroscopic applications," Measurement Science and Technology, vol. 11, pp. 392–397, 2000.

[29] R. Widenhorn, J. C. Dunlap, and E. Bodegom, "Modeling nonlinear dark current behavior in CCDs," IEEE Transactions on Electron Devices, vol. 57, pp. 581–587, 2010.

[30] R. V. Duyne, D. L. Jeanmaire, and D. F. Shriver, "Mode-locked laser Raman spectroscopy. New technique for the rejection of interfering background luminescence signals.," Applied Spectroscopy, vol. 46, pp. 213–222, 1974.

[31] R. Guntupalli, V. Hagan, A. Cooper, and R. Simpson, "New ultra-high speed CCD camera achieves sub-electron read noise using on-chip multiplication gain (EMCCD) technology," Proceedings of SPIE, vol. 5580, pp. 905–912, 2005.

[32] M. S. Robbins and B. J. Hadwen, "The noise performance of electron multiplying charge-coupled devices," IEEE Transaction on electron devices, vol. 50, pp. 1227–1232, 2003.

[33] R. Ingley, D. R. Smith, and A. D. Holland, "Life testing of EMCCD gain characteristics," Nuclear Instruments and Methods in Physics Research A, vol. 600, pp. 460–465, 2009.

[34] S. T. Balke, Quantitative Column Liquid Chromatography: A Survey of Chemometric Methods. New York, NY: Elsevier, 1994.

[35] E. Hassel, "RAMSES spectral synthesis source code," tech. rep., University of Darmstadt, Darmstadt, Germany, 1996.

[36] G. Avila, G. Tejeda, J. Fernandez, and S. Montero, "The rotational Raman spectra and cross sections of H2O, D2O, and HDO," Journal of Molecular Spectroscopy, vol. 220, pp. 259–275, 2003.

[37] P. D. G. Magnotti, A.D. Cutler, "Development of a dual-pump CARS system for measurements in a supersonic combusting free jet," 2012.

[38] P. Sabia, M. deJoannon, A. Picarelli, and R. Ragucci, "Methane auto-ignition delay times and oxidation regimes in MILD combustion at atmospheric pressure," Combustion And Flame, vol. 160, pp. 47–55, 2013.

[39] G. P. Smith, D. M. Golden, M. Frenklach, N. W. Moriarty, B. Eiteneer, M. Goldenberg, C. T. Bowman, R. K. Hanson, S. Song, W. C. Gardiner, V. V. Lissianski, and Z. Qin, "GRI." `http://www.me.berkeley.edu/gri\_mech/`, 2000.

[40] FLUENT, "User's guide v15," 2013.

[41] A. Verissimo, R. Oliveira, P. J. Coelho, and M. Costa, "Numerical simulation of a small-scale MILD combustor," Journal of Physics: Conference Series, vol. 395, pp. 503–518, 2012.

[42] I. Gran and B. F. Magnussen, "A numerical study of a bluff-body stabilized diffusion flame. part 1: Influence of turbulence modeling and boundary conditions," Combust. Sci. Technol., vol. 119, pp. 171–190, 1996a.

[43] I. Ertesvag and B. F. Magnussen, "The eddy dissipation turbulence energy cascade model," Combust. Sci. Technol., vol. 159, pp. 213–235, 2000.

[44] L. Wang, Z. Liu, S. Chen, and C. Zheng, "Comparison of global combustion mechanisms," Combust. Sci. Technol., vol. 184, 2011.

[45] P. J. Coelho and N. Peters, "Unsteady modeling of a piloted methane/air jet flame based on the *e*ulerian particle flamelet model," Combustion and Flame, vol. 124, pp. 444–465, 2001.

[46] P. J. Coelho and N. Peters, "Numerical simulation of a Mild combustion burner," Combustion and Flame, vol. 124, pp. 503–518, 2001.

[47] M. Chen, M. Hermann, and N. Peters, "Flamelet modeling of lifted turbulent methane/air and propane/air jet diffusion flame," Proc. Combust. Inst., vol. 28, pp. 167–174, 2000.

[48] H. Pitsch, M. Chen, and N. Peters, "Unsteady flamelet modeling of turbulent hydrogen-air diffusion flames," The Combustion Institute, vol. 27, pp. 1057–1064, 1998.

[49] R. Barlow, A. Karpetis, J. Frank, and J.-Y. Chen, "Scalar profiles and NO formation in laminar opposed-flow partially premixed methane/air flames," Combustion and flame, vol. 127, no. 3, pp. 2102–2118, 2001.

[50] I. Glassman, Combustion. Boston, Ma: Academic Press, 4th ed., 2008.

[51] F. L. Dryer and I. Glassman, "High temperature oxidation of CO and CH4," Fourteenth Symposium on Combustion, The Combustion Institute, p. 987, 1972.

[52] C. K. Westbrook and F. L. Dryer, "Simplified reaction mechanisms for the oxidation of hydrocarbon," Combust. Sci. Technol., vol. 27, pp. 31–44, 1981.

[53] W. Jones and R. P. Lindstedt, "Global reaction schemes for hydrocarbon combustion," Combustion and Flame, vol. 73, pp. 233–249, 1988.

[54] J. Andersen, C. L. Rasmussen, T. Giselsson, and P. Glarborg, "Global combustion mechanisms for use in CFD modeling under oxy-fuel conditions," Energy and Fuels, vol. 23, pp. 1379–1389, 2009.

[55] R. Goldstein and M. Franchett, "Heat transfer from a flat surface to an oblique impinging jet," ASME J. Heat Mass Transfer, vol. 110, pp. 87–93, 1988.

[56] L. Milne-Thomson, Theoretical Aerodynamics, By L.M. Milne-Thomson. Macmillan, 1966.

[57] J. Adeosun∗ and A. Lawal, "Numerical and experimental studies of mixing characteristics in a t-junction microchannel using residence time distribution," Chemical Engineering Science, vol. 64, pp. 2422–2432, 2009.

[58] K. G. Denbigh and J. Turner, Chemical Reactor Theory: An Introduction. New York: Cambridge University Press, 1984.

[59] J. A. Wunning and J. Wunning, "Flameless oxidation to reduce thermal NO-formation," Prog. in Energy and Comb. Sci., vol. 23, pp. 81–94, 1997.

[60] A. Cavigiolo, M. A. Galbiati, A. Effuggi, D. Gelosa, and R. Rota, "MILD combustion in a laboratory-scale apparatus," Combustion Science and Technology, vol. 175, no. 8, pp. 1347–1367, 2003.